Article

Neuronal dynamics direct cerebrospinal fluid perfusion and brain clearance

https://doi.org/10.1038/s41586-024-07108-6

Received: 16 February 2023

Accepted: 23 January 2024

Published online: 28 February 2024

Check for updates

Li-Feng Jiang-Xie[1,2]✉, Antoine Drieu[1,2,3], Kesshni Bhasiin[1,2,3], Daniel Quintero[1,2], Igor Smirnov[1,2] & Jonathan Kipnis[1,2]✉

The accumulation of metabolic waste is a leading cause of numerous neurological disorders, yet we still have only limited knowledge of how the brain performs self-cleansing. Here we demonstrate that neural networks synchronize individual action potentials to create large-amplitude, rhythmic and self-perpetuating ionic waves in the interstitial fluid of the brain. These waves are a plausible mechanism to explain the correlated potentiation of the glymphatic flow[1,2] through the brain parenchyma. Chemogenetic flattening of these high-energy ionic waves largely impeded cerebrospinal fluid infiltration into and clearance of molecules from the brain parenchyma. Notably, synthesized waves generated through transcranial optogenetic stimulation substantially potentiated cerebrospinal fluid-to-interstitial fluid perfusion. Our study demonstrates that neurons serve as master organizers for brain clearance. This fundamental principle introduces a new theoretical framework for the functioning of macroscopic brain waves.

Neuronal activity inevitably produces metabolic waste[3,4]. Billions of neurons with high metabolic turnover rates and elaborate spatial layouts are packed into the brains of higher organisms. To prevent environmental insults and stochastic autoimmunity, the brain parenchyma is further protected by the blood–brain barrier[5] and is devoid of canonical lymphatic vasculature[6]. All of these evolutionary adaptations create a problem for the brain, namely, how to dispose of its metabolic waste. Insights into this biological dilemma were provided after discovery of the glymphatic system[1,2]. Here cerebrospinal fluid (CSF) pulsates along the perivascular spaces surrounding penetrating arteries, infuses the brain parenchyma through the aquaporin-4 channels on astrocytes and flushes metabolic wastes into perivenous pathways[7]. Substantial knowledge has been acquired regarding bulk flow in perivascular spaces[8]. However, fluid dynamics within the high-resistance parenchyma (neurons, glial cells and the surrounding interstitial space together account for around 95% of the brain volume in vivo)[9] remain largely a mystery.

Within the brain, billions of neurons form complicated networks for cognitive processing. How the interstitial fluid (ISF) navigates this maze and efficiently removes brain waste is a fundamental question in neuroscience. Recent electroencephalography (EEG) studies have revealed that neural activity can be used to predict haemodynamics and CSF oscillations during sleep in humans[10], and that it correlates with glymphatic function under different brain states[2] and anaesthetic regimens[11]. Nonetheless, as these studies are largely associative in nature, a cause–effect relationship between neuronal activity and brain clearance remains to be established. Moreover, it is unclear how coarse neuronal activity, as measured through scalp or intracranial EEG recordings obtained outside the brain, correlates with CSF-to-ISF perfusion within the parenchyma.

Rhythmic ionic waves in ISF boost brain perfusion

To deepen our understanding of the potential interdependence between neuronal activity and fluid dynamics within the brain parenchyma, we performed in vivo extracellular electrophysiological recording in behaving animals while simultaneously monitoring their global brain state by EEG and electromyography (EMG)[12–14] (Fig. 1a). A sharp ultrathin silicon probe was inserted inside the hippocampus to measure neuronal spikes and extracellular field potentials. A crucial realization here was that the electrodes in these experiments are positioned outside the neurons in the interstitial space (hence, extracellular recording). As such, the field potentials recorded reflect the ionic dynamics in the ISF (Fig. 1a). Traditionally, these ionic currents have been used to infer local neural activity[14]. Here, instead of investigating how neural activity contributes to diverse cognitive tasks, we realized that one of its fundamental but unappreciated functions might be regulating brain ISF dynamics. To study the relationship between neuronal activity and brain clearance, we first utilized a ketamine anaesthesia model (intraperitoneal (i.p.) injection of 100 mg kg^{-1} ketamine with 10 mg kg^{-1} xylazine) as it has been shown to enhance the glymphatic system at a level comparable to that in natural sleep[2,11].

EEG recordings in an awake mouse are characterized by irregular fast oscillations with small swings, whereas EMG traces reflect muscle movements[15–17]. Simultaneously recorded ionic dynamics in the ISF also displayed minor fluctuations across the dorsal–ventral axis of the hippocampus (Fig. 1b, left, and Extended Data Fig. 1a,b). Under ketamine anaesthesia, the delta wave (0.5–4.0 Hz) is strongly enhanced in both parietal and frontal EEG recordings, whereas muscle activity is minimal[18,19]. Notably, large-amplitude slow oscillations interleaved with high-frequency ionic waves (10–50 Hz) began to dominate field potential recordings in the hippocampus (Fig. 1b, middle, and Extended

[1]Brain Immunology and Glia (BIG) Center, Washington University in St Louis, St Louis, MO, USA. [2]Department of Pathology and Immunology, School of Medicine, Washington University in St Louis, St Louis, MO, USA. [3]These authors contributed equally: Antoine Drieu, Kesshni Bhasiin. ✉e-mail: li-feng@wustl.edu; kipnis@wustl.edu

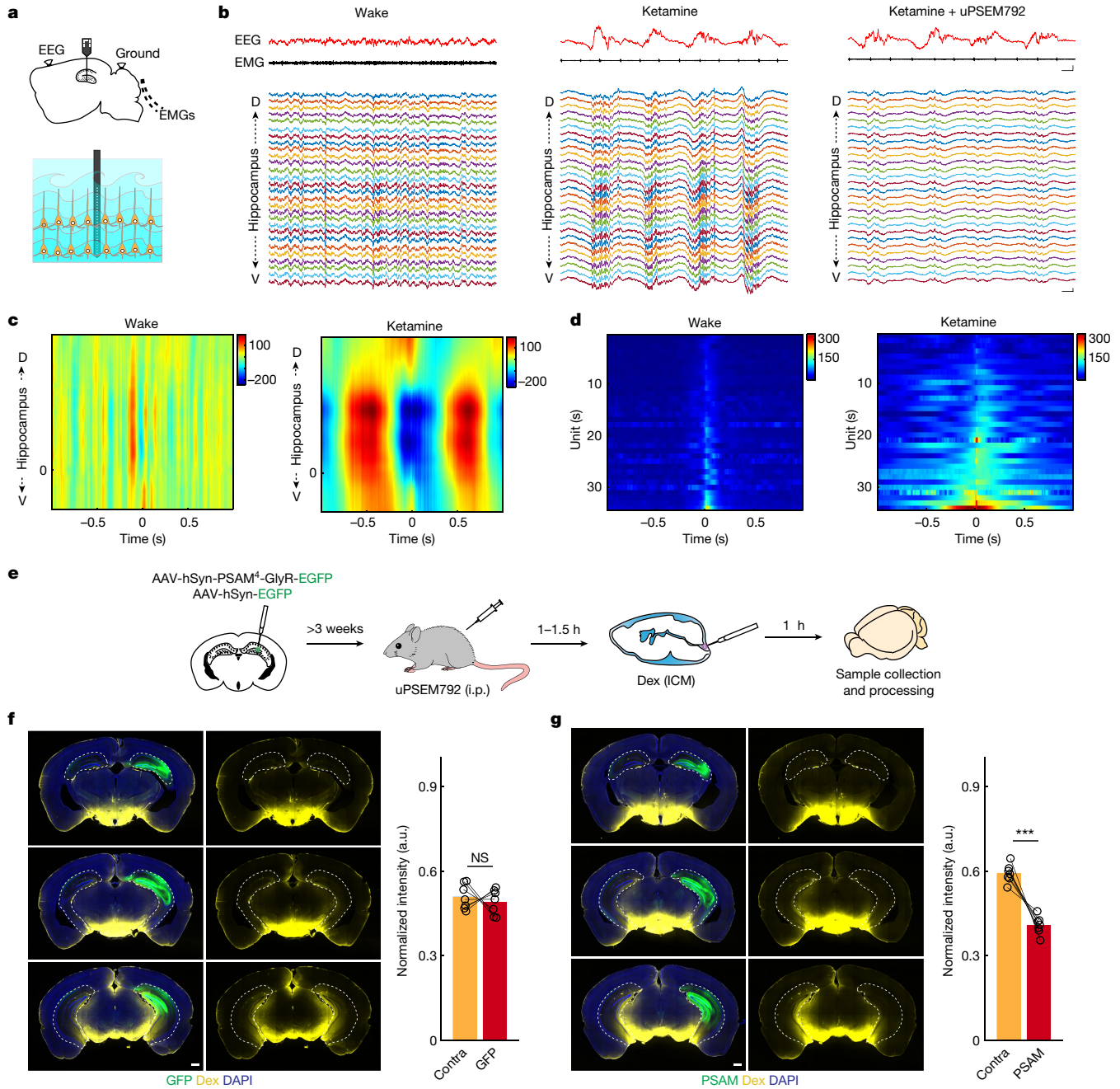

Fig. 1 | Large-amplitude and rhythmic ionic dynamics in ISF generated by neuronal synchronization during ketamine anaesthesia are required for brain CSF perfusion. a, Top, illustration of in vivo multiplexed electrophysiological recording. Bottom, representative recording of ionic flow in ISF of the hippocampus. **b**, Representative traces of EEG, EMG and ionic waves in the hippocampus during wake (left), ketamine anaesthesia (middle) and ketamine anaesthesia with chemogenetic inhibition (right) conditions. Ketamine anaesthesia was 100 mg kg^{-1} ketamine with 10 mg kg^{-1} xylazine, i.p. injection. Top right scale bar, 200 ms and 200 μV for EEG; bottom right scale bar, 200 ms and 200 μV for local field potentials (LFPs). D, dorsal; V, ventral. **c**, Representative spike-triggered field potential averaging during wake and ketamine anaesthesia conditions. The unit for the colour bar is μV. **d**, Summary of all spiking units (n = 34 units from 5 mice) and their relationship with the extracted amplitudes (Hilbert method) of field potentials. The unit for the colour bar is μV. **e**, Schematic of fluorescent CSF-to-ISF tracing with or without chemogenetic inhibition. Dex, dextran–Texas Red, 3 kDa. **f**,**g**, Images (left) and quantification (right) of CSF tracer infiltration in mice expressing control GFP (**f**; n = 7 mice) or PSAM (**g**; n = 7 mice). For the representative images, the left column displays composite images (GFP, Dex and DAPI) from anterior to posterior (top to bottom), whereas the right column demonstrates corresponding tracer-only (Dex) images. Contra, contralateral side of the hippocampus. White dashed lines highlight bilateral hippocampi. Scale bar, 500 μm. Two-sided paired t-test. P = 0.0003 in PSAM group comparison. a.u., arbitrary units; NS, not significant; ***P < 0.001.

Data Fig. 1b). Power-phase coherence analysis revealed that these two distinct rhythms were tightly coupled together (Extended Data Fig. 1c–e). In terms of wave power, high-amplitude fluctuations carry a larger potential energy, whereas fast oscillations contain a stronger kinetic energy. Such well-structured ionic dynamics under ketamine anaesthesia therefore generated strong wave energy, which, arguably, could facilitate the movement of small molecules and peptides within the interstitial space.

Utilizing in vivo electrophysiology, we were able to both record macroscopic ionic dynamics and individual spikes (action potentials) from

cells[13,14] (Extended Data Fig. 2a). Neuronal units (n = 34 across 5 animals) were reliably identified after spike-sorting[20]. Notably, neuronal activity in the hippocampus was suppressed by ketamine anaesthesia (Extended Data Fig. 2b). This result raised the question of how neurons can generate larger amplitude of ionic waves in the ISF when fewer spikes were available. To investigate the coordination between individual spikes and population activity, we performed spike-triggered field potential averaging[21] across different brain states. In awake animals, individual spikes (occurring at time = 0 and channel = 0) usually accompanied spatially restricted (y axis, channel) and temporally limited (x axis, time) fluctuations in field potentials, which typically reflect incoherent population activity in the vicinity of the recording electrodes[14] (Fig. 1c). The spikes from the same neuronal unit synchronized with large fluctuations in field potentials under ketamine anaesthesia (Fig. 1c). Across all the neuronal units that we recorded, individual spikes were always timed with larger amplitude swings in field potentials during ketamine anaesthesia (Fig. 1d and Extended Data Fig. 2c). These substantial fluctuations in field potentials typically indicate coherent activity of neural ensembles[22]. In other words, neurons fire together to generate large-amplitude ionic currents in the interstitial spaces, apparently compensating for the availability of fewer spikes under ketamine anaesthesia.

We next sought to determine whether these field potential dynamics are truly driven by neurons. To this end, we exploited recently developed chemogenetic toolkits, pharmacologically selective actuator modules coupled with glycine receptor (PSAMs–GlyR)[23], to silence neuronal activity. PSAM–GlyR was expressed in the hippocampus (Extended Data Fig. 1a), and after treatment with its synthetic ligand, ultrapotent pharmacologically selective effector molecule 792 (uPSEM792)[23], neuronal action potentials were reduced to almost undetectable levels (Extended Data Fig. 2d). As a result of such inhibition, the ISF ionic waves observed during ketamine anaesthesia were flattened, and the power across all oscillatory frequencies (0.5–55 Hz) was decreased (Fig. 1b, right, and Extended Data Fig. 1bii). Moreover, simultaneously recorded frontal and parietal EEG traces were largely identical to those seen in unsilenced controls (Fig. 1b, middle and right, and Extended Data Fig. 1bi). This result indicated that our chemogenetic inhibition strategy selectively attenuated ionic waves in a localized region (hippocampus) without affecting the global state of the brain.

The observed specificity and efficiency of chemogenetic inhibition provided an opportunity to investigate how ionic dynamics in ISF affects certain aspects of glymphatic function. To capture CSF-to-ISF perfusion, a low molecular weight tracer (dextran–Texas Red, 3 kDa)[1,2] was introduced into the CSF through intracisterna magna (ICM) injection under ketamine anaesthesia while neuronal activity was chemogenetically silenced on one side of the hippocampus (Fig. 1e). In control mice expressing GFP and given an i.p. injection of uPSEM792, the tracer (yellow) evenly perfused both hemispheres, with stronger signals in the ventral and caudal parts of the brain, producing a typical pattern of glymphatic perfusion after ICM injection[1,11] (Fig. 1f). Notably, chemogenetic inhibition impeded CSF infiltration into the hippocampus, whereas perfusion to the contralateral hippocampus was intact (Fig. 1g). Other brain regions were largely unaffected (Extended Data Fig. 3). Moreover, expression of GFAP and the integrity of the blood–brain barrier was not affected by chemogenetic neuronal silencing (Extended Data Fig. 4). These findings suggest that the rhythmic neuronal activity produced under ketamine anaesthesia is a prerequisite for brain CSF perfusion.

Neurons are highly efficient pumps, and a large proportion of their energy is used to power Na^+/K^+-ATPases[4], which reset membrane potentials within a couple of milliseconds after each spike[24]. This mechanism enables neurons to flip their membrane potentials up to about 500 times per second[25]. Although the extracellular current generated by an individual cell is negligible, neurons form networks to coordinate their actions. The synchronization of numerous neuronal pumps generates large ionic waves in the ISF, which can arguably facilitate CSF perfusion and waste clearance. Although there is currently no available experimental method to directly measure fluid flow in the ISF of behaving animals[9], water, being a polar molecule, typically forms hydration shells arounds ions. As a result, we suggest that the dynamics of ISF could be indirectly inferred by field potential recordings.

Sleep synchronizes neurons to drive brain CSF perfusion

We next sought to determine whether principles similar to those described above for ketamine anaesthesia also apply to natural sleep. To address this question, we placed a linear electrode array inside the hippocampus while monitoring the brain state with simultaneously acquired EEG and EMG recordings. As described above, wakefulness was characterized by small and irregular fluctuations in hippocampal field potentials (Fig. 2a and Extended Data Fig. 5). Notably, large-amplitude ionic waves started to appear in the hippocampus during non-rapid eye movement (NREM) sleep, as indicated by slow oscillations (0.5–4 Hz) on EEG traces and minimal muscle movements[15,17] (Fig. 2a and Extended Data Fig. 5). By contrast, rapid eye movement (REM) sleep was characterized by highly rhythmic theta oscillations (6–10 Hz) originating in the hippocampus and propagating to cortical EEG traces, whereas muscle tone was completely lost[15,17] (Fig. 2a and Extended Data Fig. 5). Sleep is known to enhance brain clearance[2,26]; therefore, we proposed that these distinct ionic dynamics in interstitial space contribute to glymphatic perfusion.

To delve into a finer scale, we quantified the spiking activity of individual neuronal units across different brain states. Notably, the spike rates of hippocampal neurons increased during sleep (Extended Data Fig. 6a–c), a result in line with previous observations[27]. It is also worth mentioning that although both sleep and ketamine anaesthesia potentiate brain clearance[2], they had the opposite effect on neuronal spiking (Extended Data Figs. 2a,b and 6a–c). Therefore, glymphatic function cannot be explained simply in terms of the amount of neuronal activity. This result raised the question of what the underlying commonality is between these two brain states.

Considering the appearance of large and rhythmic ionic fluctuations in the interstitial space during both sleep and ketamine anaesthesia, we reasoned that the underlying cause might be the temporal synchronization of neural spikes. Therefore, spike-triggered field potential averaging[21] was performed to investigate the temporal coordination between individual units and population activity. As shown above, spikes from individual units usually partnered with a spatiotemporal-restricted undulation in field potentials during wakefulness (Fig. 2b). Spiking activity from the identical unit coordinated larger amplitude swings in field potentials across recording channels during both NREM and REM sleep (Fig. 2b). Group analysis revealed that individual spikes always coincided with larger fluctuations in field potentials during slumber (Fig. 2c and Extended Data Fig. 6d). This coherent action of neuronal ensembles evidently generated stronger wave energy, which is arguably capable of propagating the movement of metabolic waste in the interstitial space.

Chemogenetic inhibition largely flattened these ionic waves in the interstitial space of the hippocampus across brain states, whereas EEG traces of the cortex were relatively intact (Extended Data Fig. 5). We therefore proceeded to explore glymphatic perfusion across different brain states as a function of neuronal activity. Initially, we validated that the animals displayed normal physiological sleep following acute ICM injection (Extended Data Fig. 7). On the day of the experiment, a low molecular weight tracer[1,2] (dextran–Texas Red, 3 kDa) was introduced into the CSF through the cisterna magna, and mice expressing PSAM–GlyR in the hippocampus were allowed to sleep freely or were kept awake by mild perturbation (Fig. 2d). In agreement with previous reports[2,26], sleep largely enhanced the penetration of tracers into the brain parenchyma (Fig. 2e,f). We next analysed how chemogenetic

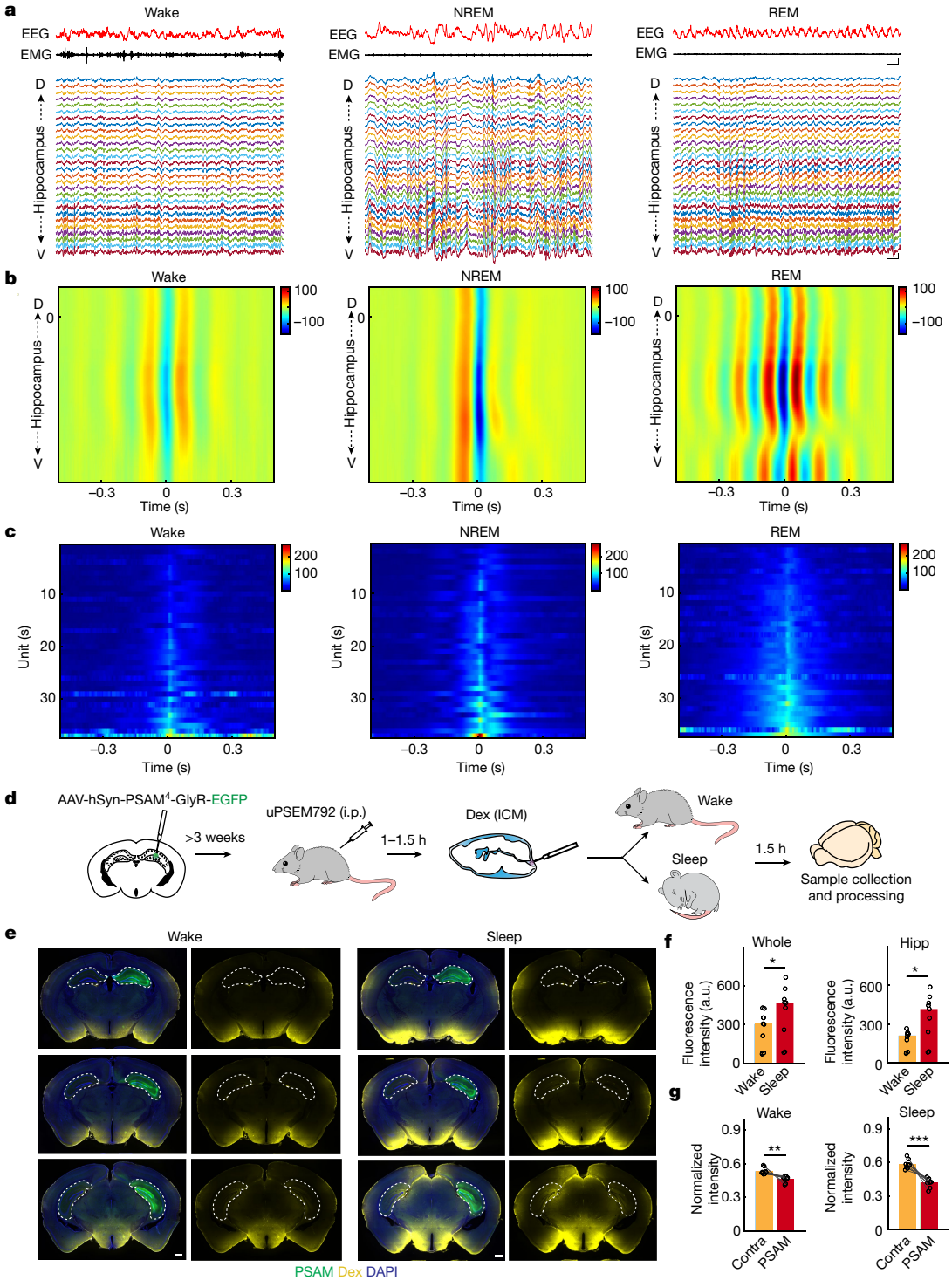

Fig. 2 | Synchronization of neuronal pumps during sleep drives high-energy ionic waves in ISF, which enhances CSF infusion. a, Representative traces of EEG, EMG and ionic waves in the hippocampus during wake, NREM and REM conditions. Top right scale bar, 200 ms and 200 μV for EEG; bottom right scale bar, 200 ms and 200 μV for LFPs. **b**, Representative spike-triggered field potential averaging during wake, NREM and REM conditions. The unit for the colour bar is μV. **c**, Summary of all spiking units ($n = 37$ units from 4 mice) and their relationship with the extracted amplitudes (Hilbert method) of field potentials. The unit for the colour bar is μV. **d**, Schematic of fluorescent CSF-to-ISF tracing with or without chemogenetic inhibition during sleep and wakefulness. **e**, The differentiated effect of chemogenetic inhibition during wakefulness and sleep. For each brain state, the left column displays composite images (GFP, Dex and DAPI) from anterior to posterior (top to bottom), whereas the right column demonstrates corresponding tracer-only (Dex) images. White dashed lines highlight bilateral hippocampi. Scale bar, 500 μm. **f**, CSF tracer intensity in whole brain slices (left) and unsilenced hippocampus (Hipp; right) under wake ($n = 10$ animals) and sleep conditions ($n = 9$ animals). Two-sided Mann-Whitney test. $P = 0.0435$ (whole slice) and 0.0172 (unsilenced hippocampus). **g**, Normalized tracer intensity between PSAM-expressing and contralateral hippocampi under wake (left, $n = 10$ mice) and sleep conditions (right, $n = 9$ mice). Two-sided paired t-test. $P = 0.0031$ (wake) and 0.0003 (sleep). $^{*}P < 0.05$, $^{**}P < 0.01$, $^{***}P < 0.001$.

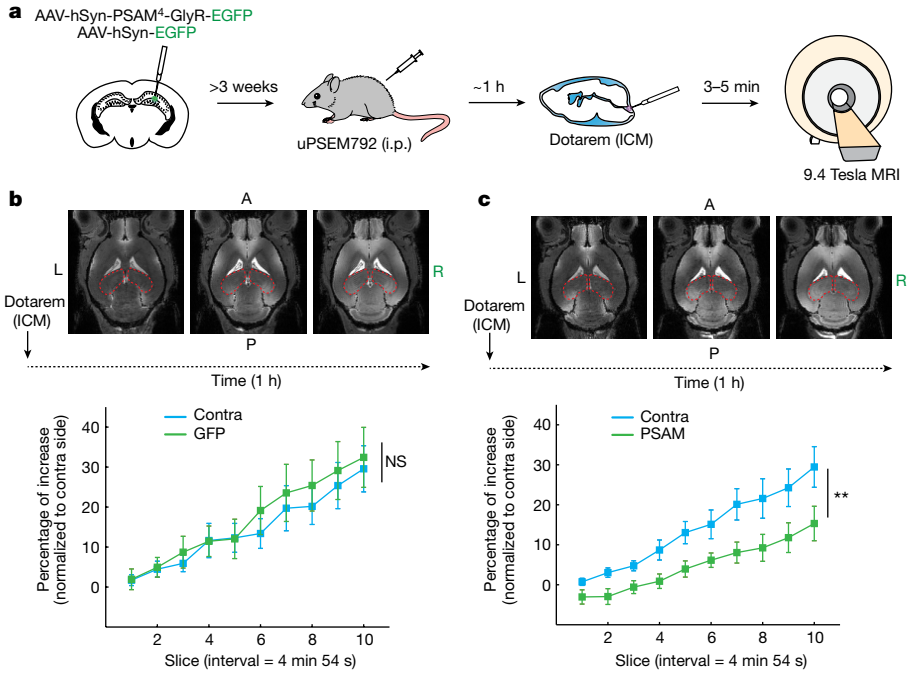

Fig. 3 | Flattening ionic waves in ISF impedes brain perfusion in vivo. **a**, Schematic of experimental procedures. Dotarem, gadolinium-based MRI contrast agent. **b**,**c**, CSF-to-ISF perfusion dynamics across time in control GFP-expressing (**b**) and PSAM-expressing (**c**) animals. Top, representative MRI images. Bottom, statistical summary. Red dashed lines highlight bilateral hippocampi. A, anterior; L, left; P, posterior; R, right. The viral vector was injected into the right side of the hippocampus. $n = 8$ (GFP) or 9 mice (PSAM). Data presented as the mean ± s.e.m. Two-way repeated-measures analysis of variance (ANOVA). $P = 0.0066$ for PSAM group comparison. $^{**}P < 0.01$.

inhibition affects CSF tracer infiltration. Inhibition of neuronal spiking attenuated CSF perfusion in the hippocampus during both wakefulness and sleep. However, the asymmetric effect across hemispheres was much larger during sleep than during wakefulness (Fig. 2e,g and Extended Data Fig. 6e), which suggested that the neuronal activity pattern during sleep is pivotal for CSF-to-ISF perfusion.

Flattened ionic waves in ISF impedes brain CSF perfusion

To capture the temporal dynamics of CSF infiltration, we performed magnetic resonance imaging (MRI)[28] of intact brains in vivo (Fig. 3a). Mice were injected with either PSAM–GlyR or control GFP vectors on one side of the hippocampus 3–5 weeks before MRI scanning. Following infusion of the small gadolinium-based contrast agent Dotarem (0.754 kDa) through the cisterna magna while under ketamine anaesthesia, animals were quickly placed inside a 9.4 Tesla Bruker scanner and their CSF influx was monitored. In control (GFP-expressing) mice, the CSF tracer gradually and evenly perfused both sides of the hippocampus, which indicated strong glymphatic function under this experimental paradigm (Fig. 3b). Ipsilateral chemogenetic inhibition of neuronal activity largely disrupted CSF-to-parenchyma perfusion, whereas the contralateral hemisphere was not affected (Fig. 3c). These results further suggest that rhythmic neuronal activity is required for brain CSF perfusion in vivo. Notably, paravascular flow remained largely unaffected when the experiment was performed using the large molecular contrast agent GadoSpin P[28], which is predominantly retained within the perivascular space (Extended Data Fig. 8a,b). These results suggest that silencing local neuronal activity in the hippocampus impedes the entry and movement of molecular tracers within the brain parenchyma.

Chemogenetic inhibition impairs brain clearance

Besides glymphatic influx, we were interested in whether neuronal activity is required for waste removal. We utilized a universal phenomenon in which molecules introduced into the CSF through ICM injection have two distinct phases (influx and efflux[1,28]; Fig. 4a). In the influx phase, the designated molecules progressively enter the brain parenchyma through CSF perfusion. Later, they are gradually cleared away through the glymphatic system during the efflux phase. Above, we demonstrated that flattening ionic waves in the interstitial space largely impedes the infiltration of molecules during the influx phase. Next, we sought to determine whether inhibition of neuronal activity also impairs molecular clearance during the efflux phase.

PSAM–GlyR or control GFP vector was expressed unilaterally in the hippocampus, and then a low molecular weight tracer (dextran–Texas Red, 3 kDa) was introduced into the CSF through ICM injection. After 3 h of glymphatic infiltration[28], the chemogenetic ligand uPSEM792 (i.p. injection) was administered to silence neuronal activity for 4 h during the efflux phase (Fig. 4b and Extended Data Fig. 8c,d). In the uPSEM792-treated GFP-expressing (control) mice, there were comparable amounts of molecules retained in the hippocampi of both hemispheres (Fig. 4c). Chemogenetic inhibition of neuronal activity during the efflux phase resulted in significantly larger quantities of molecules trapped in the hippocampus (Fig. 4d). These results indicate that neuronal activity is not only required for CSF entrance into but also for molecular clearance from the brain.

Synthesized waves enhance CSF-to-ISF perfusion

By taking advantage of newly developed transcranial optogenetics[29,30], we were able to generate synthesized ionic waves in the interstitial space (Extended Data Fig. 9a–c) without invasive fibre penetration that might disrupt fluid dynamics. ChRmine[29] or its control red fluorescence protein (RFP) was expressed on one side of the hippocampus. Following infusion of a low molecular weight tracer (dextran–fluorescein, 3 kDa) into the CSF, red light (635 nm) from a laser was delivered through a fibre placed on top of the skull during the glymphatic infiltration phase (Fig. 5a). Light stimulation was patterned to mimic the high-energy,

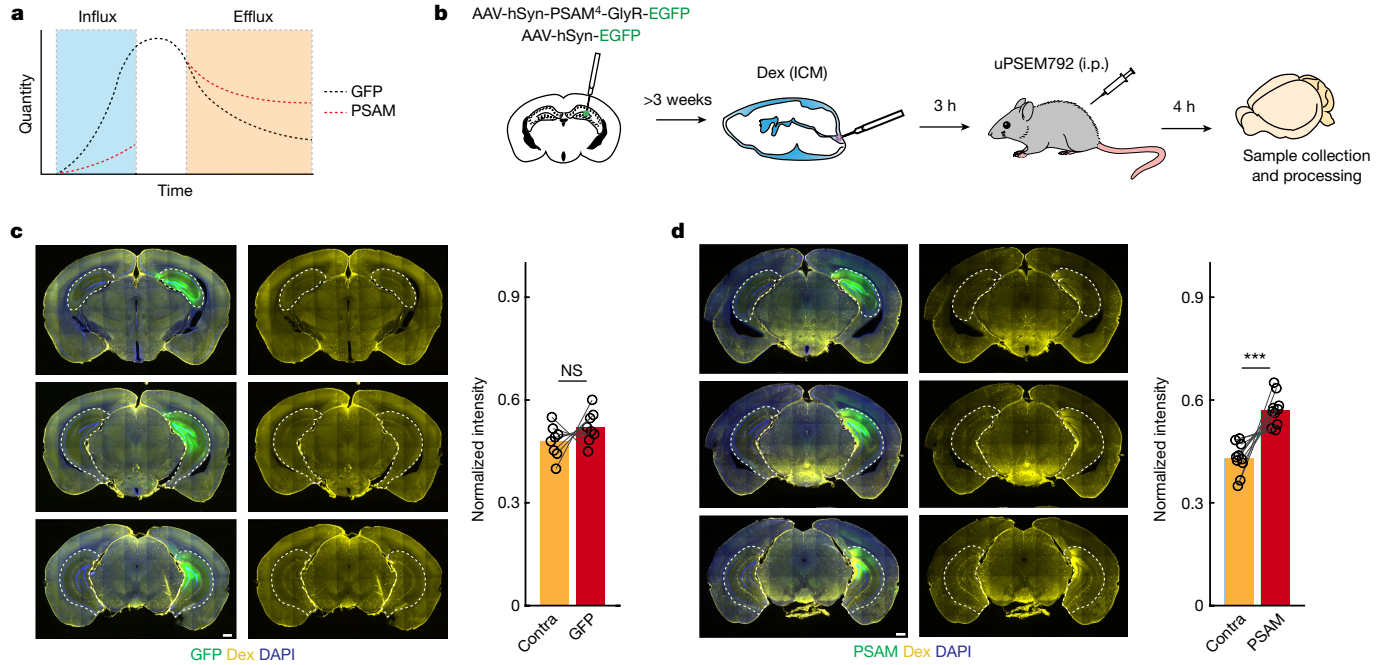

Fig. 4 | Chemogenetic inhibition of neural activity impairs brain clearance. **a**, Illustration of the glymphatic influx and efflux of designated molecules and the prediction from our working hypothesis. **b**, Schematic of viral constructs, stereotaxic injection and experimental procedures. **c**,**d**, Molecular clearance in control GFP-expressing (**c**) and PSAM-expressing (**d**) animals. For the representative images, the left column displays composite images (GFP, Dex and DAPI) from anterior to posterior (top to bottom) of the brain, whereas the right column demonstrates corresponding Dex-only images. White dashed lines highlight bilateral hippocampi. $n = 8$ (GFP) and 10 (PSAM) mice. Scale bar, 500 µm. Two-sided paired t-test. $P = 0.0009$ for PSAM group comparison. $^{***}P < 0.001$.

slow oscillation (1 Hz, 50 ms on and 950 ms off) generated during NREM sleep and anaesthesia, as well as rhythmic theta waves (8 Hz, 6.25 ms on and 118.75 ms off) observed during REM sleep (Fig. 5). The efficacy of the technology was validated by staining of the neuronal activity marker Fos. Red light strongly and selectively evoked neuronal activation in cells expressing ChRmine (Extended Data Fig. 9a). In vivo optrode recording (optogenetics coupled with in vivo extracellular recording[31]) validated that our stimulation paradigms reliably entrained slow (0.5–4 Hz) and theta (6–10 Hz) waves in hippocampal field potential recording (Extended Data Fig. 9b,c). Moreover, both slow and theta waves entrained by transcranial optogenetics largely potentiated CSF-to-ISF perfusion. This was evidenced by the larger amount of molecular tracer infiltrated in the ChRmine-expressing side of the hippocampus, whereas this asymmetry was not present in the RFP-expressing control animals (Fig. 5b,c). These results demonstrate that rhythmic brain waves generated through noninvasive optogenetic stimulation can potentiate CSF perfusion through brain parenchyma and open up a new possibility to enhance brain clearance by harnessing neural dynamics.

Discussion

Our study established a new experimental paradigm to simultaneously interrogate the influx and efflux of the glymphatic system with bidirectional neuronal perturbation without damaging the brain parenchyma. Leveraging transcranial optogenetics, 9.4 Tesla MRI scanning, multiplexed electrophysiology and fluorescent molecular tracing, we demonstrated that rhythmic neuronal oscillations serve as the master organizer of CSF-to-ISF perfusion and brain clearance.

Neuronal activity produces metabolic waste[3,4]. This begs the question of how, then, does it also mediate waste removal. The resolution to this apparent paradox resides in the pattern of neuronal activation. Firing of neurons in a highly desynchronized fashion maximizes the information complexity for diverse cognitive tasks during wakefulness[32]. However, owing to out-of-sync spiking, the field potentials generated by individual neurons cancel each other out, thereby producing only small fluctuations in the ISF. By contrast, neurons coordinate their actions to generate large-amplitude, rhythmic ionic oscillations in the ISF during sleep (or ketamine anaesthesia). These high-energy ionic waves facilitate the perfusion of fresh CSF through the parenchyma and the removal of metabolic waste products. In essence, neurons that fire together 'shower' together (Extended Data Fig. 9d).

Traditionally, the glymphatic system has been described as a physical conduit that is predominantly driven by vascular pulsations. This system allows fresh CSF to travel from the para-arterial space, flush out metabolic waste in the brain interstitial space and transport them to the perivenous space[1,7]. However, this model has been challenged by the lack of a significant pressure gradient experimentally observed between para-arterial and paravenous spaces, which would be necessary to drive convection flow through the brain parenchyma[33,34]. Our research, along with other studies[35,36], identify an important yet overlooked player: the neurons. Neurons not only have the capability to generate ionic waves in ISF but also regulate para-vascular flow through distant neurovascular coupling[36], as well as efflux transportation across the blood–brain barrier[35]. In essence, neurons are the most ideal cell type that coordinate the dynamics of paravascular flow, brain interstitial fluid and the blood–brain barrier to optimize metabolic waste clearance. Future research is required to delineate the intricate interactions between neurons and various other components (such as aquaporin-4 channels[1,2]) of the glymphatic system.

It has been widely recognized that brain waves are not merely localized events; they travel along specific spatiotemporal axes across the brain[37–39]. Local neural oscillators are organized into chains[39], which could facilitate brain waves traversing specific directions to drive fluid passage. In our electrophysiological recordings, which spanned only about 700 µm across the hippocampus, brain waves were initiated at

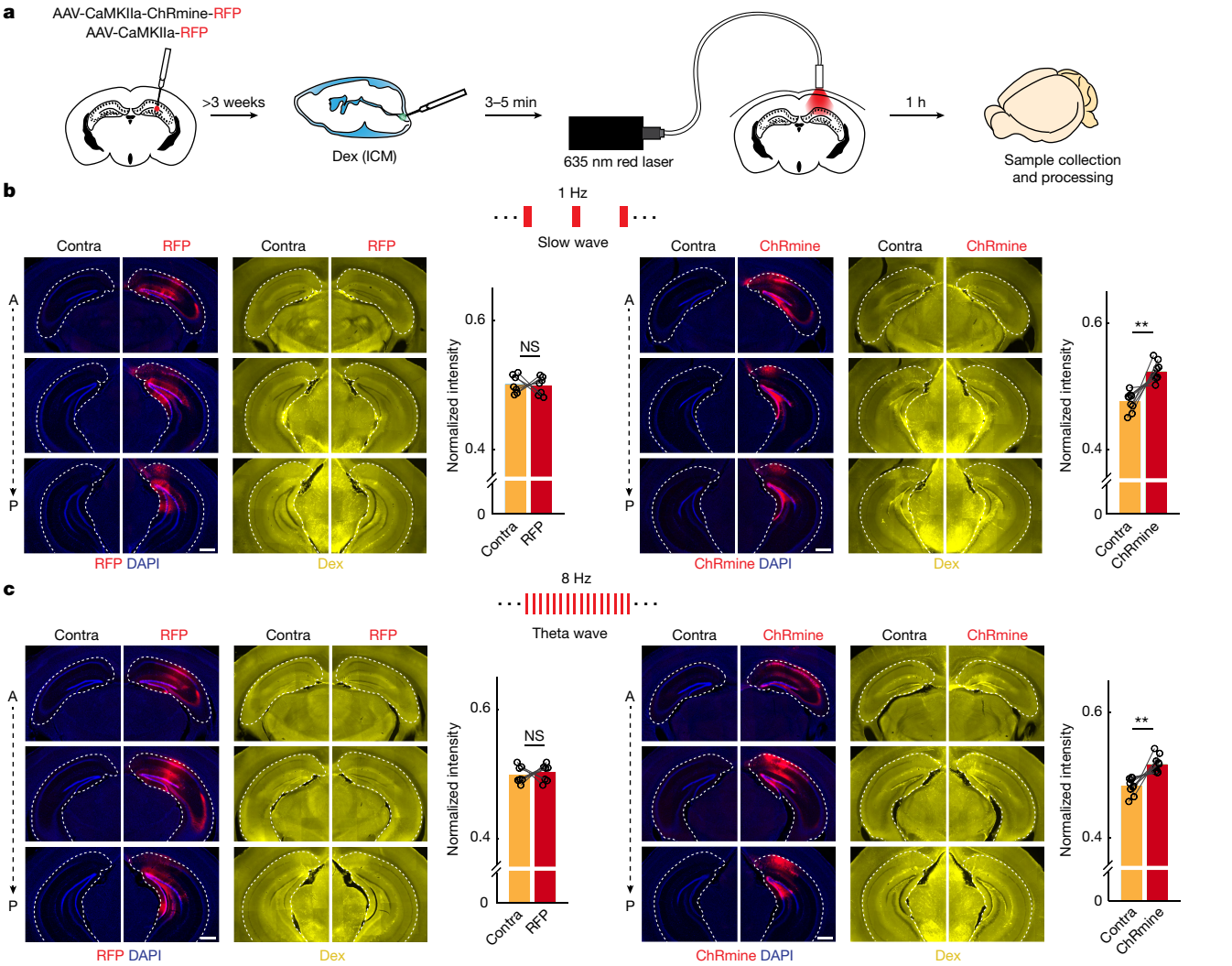

Fig. 5 | Synthesized brain waves generated by transcranial optogenetic potentiate brain CSF-to-ISF perfusion. a, Schematic of viral constructs, stereotaxic injection and experimental procedures. **b**, Rhythmic 1 Hz optogenetic stimulation on CSF-to-ISF infiltration. Left, RFP group ($n = 7$ mice). Right, ChRmine group ($n = 9$ mice). Within each panel, the left two columns display composite images (RFP or ChRmine with DAPI) from anterior to posterior (top to bottom) in vector-expressing and contralateral sides of the hippocampus, whereas the right two columns demonstrate corresponding tracer-only (Dex) images. Statistical analysis provided on the right of each panel. **c**, Rhythmic 8 Hz optogenetic stimulation on CSF-to-ISF infiltration. Left, RFP group ($n = 8$ mice). Right, ChRmine group ($n = 10$ mice). Within the panel, the left two columns show composite images (RFP or ChRmine with DAPI) from ipsilateral and contralateral sides of the hippocampus, whereas the right two columns illustrate the corresponding Dex images. White dashed lines highlight bilateral hippocampi. Scale bar, 500 μm (**b**,**c**). Two-sided paired *t*-test. $P = 0.0016$ (slow wave group) and $P = 0.0027$ (theta wave group). $^{**}P < 0.01$.

preferred locations and propagated to adjacent recording channels (Extended Data Fig. 10). Understanding how these travelling waves organize global and local fluid dynamics will be a major research direction in the coming years.

Our research, together with previous reports[11,40], also helps clarify the inconsistent results obtained across different laboratories. As glymphatic perfusion requires proper functioning of neurons, the selection of general anaesthetics is crucial. Many commonly used general anaesthetics, such as isoflurane, pentobarbital and avertin, target $GABA_A$ receptors to suppress neural activity[12]. Studies that use these anaesthetics often report a lack of significant glymphatic flow[11,41]. Another major discrepancy arises from the acute lesions in brain parenchyma caused by experimental procedures[40–42]. These injuries not only disrupt neural activity but also create 'short-circuits' that disrupt the orderly propagation of travelling waves in the brain. The experimental methodologies we used here largely avoid acute damage to the brain parenchyma, thereby providing valuable strategies for further investigations into neural dynamics and brain clearance.

Synchronization of neuronal spikes also largely increases information redundancy[43] because individual cells begin to behave similarly. This leads to an unconscious state in the nervous system, as exemplified by sleep. Not coincidentally, the sleeping brain generates the most rhythmic oscillations: delta (0.5–4 Hz), theta (6–10 Hz), spindle (12–15 Hz) and ripple (140–200 Hz) waves[22] are all well-orchestrated and temporally coupled with each other. Although the dominant frequency bands differ across species, the large and rhythmic ionic flows in the interstitial space constitute a recurring theme across the entire animal kingdom[22,44–46]. Our data presented here suggests that these neuronal waves participate in brain cleansing. It is conceivable that variations in oscillatory frequency could be tuned to the geometry of brain structures and to the physical properties (weight, charge and stickiness) of waste materials[10,47,48]. To sustain and automate waste clearance during sleep, we propose that multiple loops of recurrent circuits[49] are designed to generate self-perpetuating oscillations. Together, our findings pinpoint neurons as important drivers of brain clearance and offer a new avenue to investigate how neural

circuits are shaped by the demand of self-cleansing throughout the evolution of sleep.

Online content

Any methods, additional references, Nature Portfolio reporting summaries, source data, extended data, supplementary information, acknowledgements, peer review information; details of author contributions and competing interests; and statements of data and code availability are available at https://doi.org/10.1038/s41586-024-07108-6.

1. Iliff, J. J. et al. A paravascular pathway facilitates CSF flow through the brain parenchyma and the clearance of interstitial solutes, including amyloid β. *Sci. Transl. Med.* **4**, 147ra111 (2012).
2. Xie, L. et al. Sleep drives metabolite clearance from the adult brain. *Science* **342**, 373–377 (2013).
3. Magistretti, P. J. & Allaman, I. Lactate in the brain: from metabolic end-product to signalling molecule. *Nat. Rev. Neurosci.* **19**, 235–249 (2018).
4. Laughlin, S. B., de Ruyter van Steveninck, R. R. & Anderson, J. C. The metabolic cost of neural information. *Nat. Neurosci.* **1**, 36–41 (1998).
5. Kaplan, L., Chow, B. W. & Gu, C. Neuronal regulation of the blood–brain barrier and neurovascular coupling. *Nat. Rev. Neurosci.* **21**, 416–432 (2020).
6. Oliver, G., Kipnis, J., Randolph, G. J. & Harvey, N. L. The lymphatic vasculature in the 21st century: novel functional roles in homeostasis and disease. *Cell* **182**, 270–296 (2020).
7. Hablitz, L. M. & Nedergaard, M. The glymphatic system. *Curr. Biol.* **31**, R1371–R1375 (2021).
8. Rasmussen, M. K., Mestre, H. & Nedergaard, M. Fluid transport in the brain. *Physiol. Rev.* **102**, 1025–1151 (2022).
9. Lei, Y., Han, H., Yuan, F., Javeed, A. & Zhao, Y. The brain interstitial system: anatomy, modeling, in vivo measurement, and applications. *Prog. Neurobiol.* **157**, 230–246 (2017).
10. Fultz, N. E. et al. Coupled electrophysiological, hemodynamic, and cerebrospinal fluid oscillations in human sleep. *Science* **366**, 628–631 (2019).
11. Hablitz, L. M. et al. Increased glymphatic influx is correlated with high EEG delta power and low heart rate in mice under anesthesia. *Sci. Adv.* **5**, eaav5447 (2019).
12. Jiang-Xie, L. F. et al. A common neuroendocrine substrate for diverse general anesthetics and sleep. *Neuron* **102**, 1053–1065.e4 (2019).
13. Buzsaki, G. Large-scale recording of neuronal ensembles. *Nat. Neurosci.* **7**, 446–451 (2004).
14. Buzsaki, G., Anastassiou, C. A. & Koch, C. The origin of extracellular fields and currents—EEG, ECoG, LFP and spikes. *Nat. Rev. Neurosci.* **13**, 407–420 (2012).
15. Scammell, T. E., Arrigoni, E. & Lipton, J. O. Neural circuitry of wakefulness and sleep. *Neuron* **93**, 747–765 (2017).
16. Buzsaki, G. & Draguhn, A. Neuronal oscillations in cortical networks. *Science* **304**, 1926–1929 (2004).
17. Weber, F. & Dan, Y. Circuit-based interrogation of sleep control. *Nature* **538**, 51–59 (2016).
18. Akeju, O. & Brown, E. N. Neural oscillations demonstrate that general anesthesia and sedative states are neurophysiologically distinct from sleep. *Curr. Opin. Neurobiol.* **44**, 178–185 (2017).
19. Chauvette, S., Crochet, S., Volgushev, M. & Timofeev, I. Properties of slow oscillation during slow-wave sleep and anesthesia in cats. *J. Neurosci.* **31**, 14998–15008 (2011).
20. Steinmetz, N. A. et al. Neuropixels 2.0: a miniaturized high-density probe for stable, long-term brain recordings. *Science* https://doi.org/10.1126/science.abf4588 (2021).
21. Destexhe, A., Contreras, D. & Steriade, M. Spatiotemporal analysis of local field potentials and unit discharges in cat cerebral cortex during natural wake and sleep states. *J. Neurosci.* **19**, 4595–4608 (1999).
22. Buzsáki, G. *Rhythms of the Brain* (Oxford Univ. Press, 2006).
23. Magnus, C. J. et al. Ultrapotent chemogenetics for research and potential clinical applications. *Science* https://doi.org/10.1126/science.aav5282 (2019).
24. Luo, L. *Principles of Neurobiology* 2nd edn (Garland Science, 2020).
25. Turecek, J., Lehnert, B. P. & Ginty, D. D. The encoding of touch by somatotopically aligned dorsal column subdivisions. *Nature* **612**, 310–315 (2022).
26. Eide, P. K., Vinje, V., Pripp, A. H., Mardal, K. A. & Ringstad, G. Sleep deprivation impairs molecular clearance from the human brain. *Brain* **144**, 863–874 (2021).
27. Miyawaki, H. & Diba, K. Regulation of hippocampal firing by network oscillations during sleep. *Curr. Biol.* **26**, 893–902 (2016).
28. Iliff, J. J. et al. Brain-wide pathway for waste clearance captured by contrast-enhanced MRI. *J. Clin. Invest.* **123**, 1299–1309 (2013).
29. Chen, R. et al. Deep brain optogenetics without intracranial surgery. *Nat. Biotechnol.* **39**, 161–164 (2021).
30. Marshel, J. H. et al. Cortical layer-specific critical dynamics triggering perception. *Science* https://doi.org/10.1126/science.aaw5202 (2019).
31. Anikeeva, P. et al. Optetrode: a multichannel readout for optogenetic control in freely moving mice. *Nat. Neurosci.* **15**, 163–170 (2011).
32. Harris, K. D. & Thiele, A. Cortical state and attention. *Nat. Rev. Neurosci.* **12**, 509–523 (2011).
33. Smith, A. J. & Verkman, A. S. The "glymphatic" mechanism for solute clearance in Alzheimer's disease: game changer or unproven speculation? *FASEB J.* **32**, 543–551 (2018).
34. Hladky, S. B. & Barrand, M. A. The glymphatic hypothesis: the theory and the evidence. *Fluids Barriers CNS* **19**, 9 (2022).
35. Pulido, R. S. et al. Neuronal activity regulates blood–brain barrier efflux transport through endothelial circadian genes. *Neuron* **108**, 937–952.e7 (2020).
36. Holstein-Ronsbo, S. et al. Glymphatic influx and clearance are accelerated by neurovascular coupling. *Nat. Neurosci.* **26**, 1042–1053 (2023).
37. Massimini, M., Huber, R., Ferrarelli, F., Hill, S. & Tononi, G. The sleep slow oscillation as a traveling wave. *J. Neurosci.* **24**, 6862–6870 (2004).
38. Lubenov, E. V. & Siapas, A. G. Hippocampal theta oscillations are travelling waves. *Nature* **459**, 534–539 (2009).
39. Zhang, H. & Jacobs, J. Traveling theta waves in the human hippocampus. *J. Neurosci.* **35**, 12477–12487 (2015).
40. Mestre, H. et al. Aquaporin-4-dependent glymphatic solute transport in the rodent brain. *eLife* https://doi.org/10.7554/eLife.40070 (2018).
41. Smith, A. J., Yao, X., Dix, J. A., Jin, B. J. & Verkman, A. S. Test of the 'glymphatic' hypothesis demonstrates diffusive and aquaporin-4-independent solute transport in rodent brain parenchyma. *eLife* https://doi.org/10.7554/eLife.27679 (2017).
42. Pla, V. et al. A real-time in vivo clearance assay for quantification of glymphatic efflux. *Cell Rep.* **40**, 111320 (2022).
43. Tononi, G. & Edelman, G. M. Consciousness and complexity. *Science* **282**, 1846–1851 (1998).
44. Shein-Idelson, M., Ondracek, J. M., Liaw, H. P., Reiter, S. & Laurent, G. Slow waves, sharp waves, ripples, and REM in sleeping dragons. *Science* **352**, 590–595 (2016).
45. Yap, M. H. W. et al. Oscillatory brain activity in spontaneous and induced sleep stages in flies. *Nat. Commun.* **8**, 1815 (2017).
46. Leung, L. C. et al. Neural signatures of sleep in zebrafish. *Nature* **571**, 198–204 (2019).
47. Iaccarino, H. F. et al. Gamma frequency entrainment attenuates amyloid load and modifies microglia. *Nature* **540**, 230–235 (2016).
48. Martorell, A. J. et al. Multi-sensory gamma stimulation ameliorates Alzheimer's-associated pathology and improves cognition. *Cell* **177**, 256–271.e22 (2019).
49. Luo, L. Architectures of neuronal circuits. *Science* **373**, eabg7285 (2021).

Methods

Animals

Adult C57BL/6 mice (Jackson Laboratory, 000664) aged 2–6 months were used in this study. Animals were randomly assigned to experimental and control groups. They were housed inside a temperature-controlled (22 °C) and humidity-controlled (33–39%) environment with a standard 12 h–12 h light–dark cycle and provided with food and water ad libitum. All experimental procedures were approved by the Institutional Animal Care and Used Committee in Washington University School of Medicine.

Stereotaxic injection and viral vectors

Mice were placed and secured in stereotaxic instruments (Kopf) under isoflurane anaesthesia (5% for induction, 1.2–1.5% for maintenance), and an ophthalmic solution was applied to protect the eye from dehydration. The fur on top of the scalp was cleaned with 70% ethanol and shaved. A small craniotomy was made on top of the parietal cortex (anterior–posterior (AP): −2.7; medial–lateral (ML): 2.5). Viral vectors (800 nl) were loaded into a Nanoliter 2020 (World Precision Instruments) with a fine glass capillary and injected into the hippocampus (AP: −2.7, ML: 2.5, and 1.5 below the surface of the brain) at the speed of 100 nl min^{-1}. After the injection, we waited an extra 8–10 min before withdrawal of the glass capillary. Analgesics were given subcutaneously, and the mice were placed on top of a heating pad until emergence from general anaesthesia. For the neuronal activity silencing experiment, PSAM4-GlyR (119742-AAV5) and its control, EGFP (50465-AAV5), were acquired through Addgene vector service. For optogenetic activation experiments, CaMKIIa-ChRmine-mScarlet (130991) and CaMKIIa-mScarlet (131000) were acquired from Addgene.

ICM injection

For glymphatic infiltration and clearance experiments (Figs. 1, 3 and 4), animals were anaesthetized with a ketamine–xylazine cocktail (100 mg kg^{-1} ketamine with 10 mg kg^{-1} xylazine, i.p. injection) during ICM injections. For the tracer infiltration experiments with sleep–wake perturbation (Fig. 2) and transcranial optogenetics (Fig. 5), brief isoflurane (1–1.5%) exposure was chosen to guarantee rapid recovery from injection procedures. Mice were secured in a stereotaxic frame. The skin on the back of the neck was cleaned with 70% ethanol and shaved with a razor blade. A small incision was made on the skin and the muscle layers were gently retracted to expose the cisterna magna. Fluorescent tracers (10 mg ml^{-1}, dextran–Texas Red, 3 kDa, Invitrogen, D3328, and 10 mg ml^{-1}, dextran–fluorescein, 3 kDa, Invitrogen, D3306) or MRI contrast agents[28,50] (Dotarem, 0.754 kDa, 0.5 mmol ml^{-1}, Guerbet; GadoSpin P, 200 kDa, 0.18 mM, Miltenyi Biotec) were loaded into a Nanoliter (World Precision Instruments) with a glass capillary. After slowly penetrating the membrane on top of the cisterna magna, the molecules were infused at the speed of 2 µl min^{-1} for 2 min. An extra 2–3 min was added before withdrawal of the glass capillary.

Tissue processing and widefield imaging for molecular infiltration and clearance

For most of the glymphatic influx studies, animals were euthanized at 1 h after ICM injection. For the molecular infiltration with sleep–wake behaviour perturbation experiment, the animals were euthanized at 1.5 h after ICM injection. For brain clearance experiments, mice were euthanized at 4 h after the treatment of chemogenetic ligands (uPSEM792, 3 mg kg^{-1}, i.p. injection). Animals were deeply anaesthetized and transcardially perfused with a small volume (5–10 ml) of PBS (pH 7.4) to quickly remove red blood cells, which contribute to background autofluorescence, followed by 4% paraformaldehyde (PFA) in PBS to fix the tissues as well as to retain the tracers. The brains were carefully dissected out and post-fixed overnight at 4 °C, then transferred into 30% sucrose PBS buffer for 2 days. Samples were further frozen in Tissue-Tek OCT compound (Sakura) and sliced at 80 µm using a cryostat (Leica Biosystems). For reconstruction of the electrode location, a finer section (40 µm) was used. Brain slices were stained with DAPI and images were acquired using Olympus Slideview VS200.

Regions of interest (ROIs) were identified and chosen based on the standard mouse brain atlas (Paxinos and Franklin's the Mouse Brain in Stereotaxic Coordinates[51]). The mean pixel intensity for each ROI was quantified using Fiji (ImageJ). To compare CSF tracer penetration across both hemispheres, mean intensity values were averaged to calculate the proportion of tracer found in each hemisphere. For each animal, 3–4 independent brain slices containing the hippocampus with about 300 µm distance apart were calculated and averaged to estimate the CSF perfusion and molecular clearance. The following additional brain regions (Extended Data Fig. 3) were selected to evaluate the locality of experimental effects: the posterior dorsal cortex, the posterior ventral cortex and the hypothalamus were chosen on the same slices for hippocampal analysis; the anterior dorsal and the ventral cortex were chosen on the brain coronal slices immediately anterior to the hippocampus. For a small set of experiments that required direct comparisons of raw fluorescence intensity across animals (sleep versus wake glymphatics, and glymphatic perfusion at 3 h and 7 h after ICM injection), extra care was taken to ensure that the identical batch of tracer was used, identical tissue processing time was used across batches of animals, and samples from different batches were imaged as closely together in time as possible. Data analysis was performed by researchers blinded to the experimental treatments.

Fos and GFAP immunofluorescence

After slices were obtained from a cryostat (Leica Biosystems), brain sections were washed with PBS twice, incubated with 1% Triton in PBS at room temperature for 1 h and blocked with normal donkey serum (NDS; Jackson Immunoresearch, 017-000-121) solution (5% NDS in PBS with 0.3% Triton X-100) at room temperature for 1 h. Sections were later incubated with the c-Fos (9F6) primary antibody (1:1,000, Cell Signaling Technology, 2250) or GFAP (1:600, Agilent Technologies, Z033429-2) at 4 °C overnight. After washing three times with PBS (20 min each at room temperature), brain sections were incubated with secondary antibody (1:300, Alexa Fluor 647 donkey anti-rabbit, Jackson Immunoresearch, 711-607-003) at 4 °C overnight. The sections were later washed three times with PBS, mounted and coverslipped. Images were acquired using an Olympus Slideview VS200. The number of Fos^+ cells and the mean intensity of GFAP signals in the hippocampus were quantified using Fiji (ImageJ).

uPSEM792 preparation and dosage

uPSEM792 was dissolved in physiological saline and administered to animals by i.p. injection at a dosage of 3 mg kg^{-1} as previously described[23]. For the CSF infiltration experiments, uPSEM792 was administered 1–1.5 h before ICM injection. To evaluate the impact of acute neuronal inhibition on blood–brain barrier integrity and GFAP signals, uPSEM792 was given 1.5–2 h before killing the animals. For the molecular clearance experiment, uPSEM792 was administered 4 h before the collection of brain samples.

Blood–brain barrier permeability assays

Animals were anaesthetized using a ketamine–xylazine cocktail (100 mg kg^{-1} ketamine with 10 mg kg^{-1} xylazine, i.p. injection). The small molecular tracer EZ-Link Sulfo-NHS-LC Biotin[52] (Thermo Fisher Scientific, 21335, 0.44 kDa) was prepared at a concentration of 100 mg ml^{-1} and administered to the animals through retro-orbital injections (75 µl per mouse). Following 5–10 min of blood circulation, the animals were quickly euthanized, and their brains were swiftly collected and post-fixed in 4% PFA overnight. The samples were subsequently transferred into 30% sucrose PBS buffer for 2 days, embedded in Tissue-Tek OCT compound (Sakura) and sectioned using a cryostat (Leica Biosystems). Brain slices were further incubated with streptavidin-conjugated

Alexa Fluor 647 (1:300, Thermo Fisher Scientific, S32357) for 1 h and stained with DAPI. Images were acquired using an Olympus Slideview VS200. The tracer coverage in the hippocampus was quantified using Fiji (ImageJ) based on the threshold method.

MRI

Gadolinium-based MRI contrast agents, Dotarem (0.754 kDa, 0.5 mmol ml^{-1}, Guerbet) or GadoSpin P (200 kDa, 0.18 mM, Miltenyi Biotec), was introduced into the CSF through ICM injection (injection volume of 4 µl; injection speed of 2 µl min^{-1}) under ketamine anaesthesia (100 mg kg^{-1} ketamine with 10 mg kg^{-1} xylazine). Mice were quickly placed inside the MRI device (9.4 Tesla MRI, Bruker Biospin), and a light dose of isoflurane (0.5–0.7%) was supplemented through a nose mask to stabilize animals during imaging acquisition. The respiratory rate was monitored, and body temperature was maintained through a heating pad. A series of T1 Flash-3D-weighted images were taken to visualize CSF perfusion with the following parameters: repetition time = 30 ms; echo time = 8 ms; number of echo images = 1; number of averages = 1; number of repetitions = 11; scan time = 4 min 54 s; flip angle = 20; field of view = 1.6 × 1.6 × 0.8 cm with a 128 × 128 × 64 matrix; spatial resolution = 125 × 125 × 125 µm (8 pixels per mm; voxel size = 0.125 mm^3); number of slices = 64; receiving coil = 4-channel brain probe. The total acquisition time was of about 1 h per mouse. Movements were corrected using the standard Advanced Normalization tools package, and the ROIs were segmented through ITK-SNAP software. For the Dotarem experiment, the mean intensity of ROIs was calculated across entire time series and normalized with the non-injected side of the hippocampus of the first image to facilitate comparison between animals. To estimate perivascular flow, GadoSpin P was introduced through ICM injection, and the ROIs were located on the major vascular pathways surrounding the hippocampus. The mean intensity was calculated and normalized with the first image of non-injected (contralateral) side. Data acquisition and analysis were performed by researchers blinded to the experimental treatments.

Behavioural manipulation of sleep and wake states

Mice were individually housed in automated sleep perturbation chambers (Pinnacle Technology, 8229) 2–3 days before the experiment with water and food ad libitum. These chambers were placed within sound-attenuation boxes (Med Associates, ENV-018SA) with a controlled 12 h–12 h light–dark cycle. Experiments were performed under the light phase when the animals have a naturally higher sleep pressure. A bar located at the bottom of the cage rotated at a very low speed (about 3 r.p.m.) to keep the animal awake for 1.5 h. The control animals were housed in identical chambers and environments without bar rotation.

Optogenetic stimulation

Three weeks after injection of the viral vectors into the hippocampus, mice were quickly anaesthetized with isoflurane and placed on a stereotaxic frame. After an incision was made on the scalp, a 400-µm diameter optical fibre (R-FOC-L400C22NA, RWD) was anchored on top of the cranium and secured with dental cement[53]. An extra 1 week was given for the animals to recover from surgery. After infusion of CSF tracer (dextran–fluorescein, 3 kDa, Invitrogen, D3306) through the cisterna magna, mice were placed inside a behaviour box (Med Associates, ENV-018SA), and their fibre cannulas were interfaced with a patch fibre (MFP_200/220/900-0.22, Doric Lenses) through mating sleeves (ADAL4, Thorlabs). To avoid restraining animal behaviour, an optic rotary joint (RJ1, Thorlabs) was connected to the patch fibre and placed on top of the behaviour box. Red light (1 Hz, 50 ms on and 950 ms off; 8 Hz, 6.25 ms on and 118.75 ms off; TTL) was delivered through the rotary joint by a 635 nm laser (MRL-III-635L, Opto Engine) and the output power was set to 50–80 mW mm^{-2} according to a previous publication[29]. One hour later, the animals were quickly euthanized, and their brains were collected for analysing tracer perfusion.

Electrophysiology surgery

Mice were anaesthetized with Isoflurane and placed on a stereotaxic frame. After making an incision on the scalp, three stainless steel screws were placed on top of the frontal, parietal and cerebellar cortices as EEG electrodes. To record the LFPs, a small craniotomy was made on top of the parietal cortex (AP: −2.5; ML: 2.0), the underlying dura was slightly removed, a linear silicon probe (NeuroNexus, A1x32-5mm-25-177-CM32) with custom EEG and EMG leads slowly penetrated the underlying cortex and was gently inserted (100 µm min^{-1}) into the hippocampus to cover the entire dorsal–ventral axis. Two thin wires were inserted into neck muscles as EMG electrodes. For experiments that required optical stimulation, a 400-µm diameter optical fibre (R-FOC-L400C22NA, RWD) was placed on top of the skull and next to the silicon probe. For experiments that only involved EEG and EMG recording, commercially available EEG and EMG headmounts (Pinnacle Technology, 8201-SS) were used. The entire implants were further secured using Metabond. Analgesics were given subcutaneously. The animals were placed on a heating pad until emergence from general anaesthesia. Mice were allowed to recover for at least 10 days before the formal experiments.

Multiplexed electrophysiology recording and analysis

Animals were habituated in a sound-attenuation cubicle with DC-powered light and fan (Med Associates, ENV-018SA) at least 3 days before the actual recording. Lightweight headstages (C3314, Intan Technology) were interfaced with silicon probe implants, and the electrophysiology signals were transmitted to an acquisition system (RZ2-2, Tucker-Davis Technologies (TDT)) through a motorized commutator (ACO32, TDT) and a subject interface (SI4, TDT). EEG, EMG and LFPs were acquired at 2,035 Hz with a 0.1 Hz high-pass filter and a 500 Hz low-pass filter, whereas neuronal spikes were recorded at 24,414 Hz using Synapse software (TDT).

For the ketamine anaesthesia experiment, mice were allowed to behave freely for the first 2 h of recording to establish the baseline sleep–wake cycle and neuronal spike rates. Saline or uPSEM792 (3 mg kg^{-1}) was given by i.p. injection afterwards. Mice were given 1 h to recover from the stress of the injection procedure and for the efficacy of chemogenetics to achieve its steady state. Quickly after the injection (i.p.) of ketamine–xylazine cocktail, the EEG and EMG recordings, hippocampal LFPs and neuronal spikes were continued to be monitored for another 2 h. For the natural sleep–wake cycle experiment, animals also behaved freely for the first 2 h as the baseline. Then, saline or uPSEM792 (3 mg kg^{-1}) was given to the mice acutely. About 1 h after the injection, the electrophysiology signals were acquired for a couple (>5) of hours.

Field potentials. A notch filter was first applied to EEG, EMG and hippocampal field potentials to attenuate the external 60 Hz electrical noise. The brain state was semi-automatically annotated with 4-s epochs using a custom-written Matlab code (MathWorks) as previously described[12]. Non-REM sleep was defined as strong delta (1–4 Hz) oscillations in the EEG traces and minimal EMG activity. REM sleep was defined as high theta (6–10 Hz) power in the EEG traces with muscle atonia. Wakefulness was identified as small amplitude and high-frequency oscillations in EEG traces with tonic EMG activity. General anaesthesia was determined by strongly enhanced slow-delta (0.5–4 Hz) oscillations in EEG traces and a complete loss of muscle tone[12,15,17].

Power spectrum. EEG and hippocampal LFP power spectra were calculated for consecutive 4-s windows within the frequency range of 0–55 Hz using fast Fourier transform (FFT). Epochs with large movement artefacts were removed from the spectrum analysis. For the ketamine anaesthesia experiment, the spectra of wakefulness were generated based on the first 2-h baseline period (median of all corresponding wake epochs), whereas the spectra of ketamine anaesthesia

with saline or uPSEM792 were generated after the mice were subjected to general anaesthesia for 1 h. For natural sleep experiments with or without uPSEM792, the power spectra of wake, NREM and REM were generated from the 2-h baseline, whereas the power spectra of wake with uPSEM792, NREM with uPSEM792, and REM with uPSEM792 were calculated from 1–3 h (2-h duration) after uPSEM792 administration. The 95% confidence intervals for EEG power spectra (n = 4–5 animals) were generated based on the t distribution[54], whereas the bootstrap method (with 10,000 iterations) was used for the spectra of hippocampal electrodes (n > 100 channels from 4–5 animals).

Cross-frequency coupling. The analysis was performed as previously described[55,56]. In brief, low-frequency (0.5–4 Hz) and high-frequency (10–50 Hz) bands were chosen based on the power spectra of hippocampal field potentials under ketamine anaesthesia. The filter kernels were constructed based on the Matlab function firls. After filtering the original time series using the Matlab function filtfilt, the instant phase of slow oscillation and the amplitude of fast waves were estimated using Hilbert transform. The relationship between phase and amplitude was further illustrated with a polar plot.

Wave phase progression across recording channels. Band pass filters (Matlab, firls) were constructed to extract slow (0.5–4 Hz) oscillations in ketamine anaesthesia and NREM sleep, as well as theta (6–10 Hz) waves in REM sleep. Their phases were further estimated using the Hilbert method and plotted according to the spatial location of the recording channels in the heatmap. To quantify the phase shift, the most dorsal electrode was selected as the reference channel. The phase difference in each channel across all corresponding brain states was summarized as an average value in polar space.

Spike. Spike-sorting was performed automatically using Kilosort (v.2.5)[20] with a template-match algorithm and curated using Phy GUI[57] if necessary. Waveforms with distinct characteristics of neuronal spikes, a clear refractory period in autocorrelogram and a good separation in feature spaces were classified as single-unit, whereas waveforms with typical spike shapes but without a clear refractory period in the autocorrelogram were classified as multiunit. To compare the spike rate across different brain states and experimental treatments, total spike counts for each unit (including single unit and multiunits) under particular brain states (determined by EEG and EMG as described above) and treatments were summed and divided by the total duration of the corresponding conditions. To facilitate comparison between individual units on the heatmap, the spike rate of each unit was further normalized with the average spike rate during the baseline 2-h recording.

Spike-triggered field potential averaging. The field potentials (typically, n = 28) across the hippocampus during particular brain states (wake, sleep, ketamine anaesthesia as indicated by EEG and EMG) were averaged channel-by-channel in reference to the spike times of a particular neuronal unit (single unit and multiunit). Each unit had its own 2D heatmap map demonstrating how its action potentials corresponded with population activity in terms of spatial (y axis, 28 recording channels spanning from the top to the bottom of the hippocampus) and temporal (x axis, x = zero, indicating spike occurrences) scales. For illustration purposes, the 2D heatmaps of demonstration units (Figs. 1c and 2b) were further interpolated with the spline method on the spatial domain (y axis). To compare across different units, the amplitudes of field potentials were extracted using Hilbert transform channel-by-channel and averaged together. The instant amplitude of field potentials for each unit (x = 0 when the spike occurred) was used for further statistical analysis.

Analysis of the duration of chemogenetic inhibition. To characterize the efficacy of chemogenetic inhibition over time, we selected three time windows: baseline (−2 to 0 h), 1–3 h and 3–5 h after uPSEM792 administration. Our experimental perturbations typically occurred from 1 to 4 h after uPSEM792 administration, and the selected time windows encompass the entire duration of the experimental manipulations. Within each time window, brain states were annotated based on EEG and EMG recordings as previously described[12,15,17]. LFPs were analysed using FFT, and the median value was calculated across all corresponding windows within each brain state. Power values ranging from 0.5 Hz to 55 Hz were aggregated to estimate the broadband power of LFPs. Two channels (2 out of 111 channels, 1.8%) were removed for further analysis owing to the decay of signal quality during such long-term electrophysiological recordings (about 7 h). The 95% confidence intervals for broadband powers across the three different time windows were determined using the bootstrap method (with 10,000 iterations).

Optrode recording. Animals were allowed to behave freely for the first hour to establish a baseline recording. Slow (1 Hz, 50 ms per pulse, 1 h) and theta (8 Hz, 6.25 ms per pulse, 1 h) stimulations were delivered using a 635 nm laser (MRL-III-635L, Opto Engine) through a motorized commutator. To extract and quantify the neural oscillations induced by optogenetics, band pass filters were constructed to isolate slow (0.5–4 Hz) and theta (6–10 Hz) waves from the field potential recordings. The filter kernels were built using the Matlab function firls. The time series were further filtered using the Matlab function filtfilt, and the power was estimated using the Hilbert method.

EEG and EMG characterization immediately after ICM

Following the recovery period of at least 10 days after EEG and EMG implantation, a small molecule tracer, dextran–Texas Red (4 µl; 10 mg ml^{-1}, 3 kDa, Invitrogen, D3328) was introduced into the CSF by ICM injection under acute isoflurane (1–1.5%) anaesthesia with analgesics administered subcutaneously. Immediately after the injection, mice were placed in EEG–EMG recording chambers. Data were acquired using a 3-channel EEG–EMG system from Pinnacle Technology (8200-K1-SL) at 1,000 Hz. Brain states were annotated as described above and previously[12,15]. Non-REM sleep was characterized by enhanced delta (1–4 Hz) waves in the EEG trace with minimal EMG muscle activity. REM sleep was defined as pronounced theta (6–10 Hz) oscillations in the EEG trace paired with muscle atonia. Wakefulness was marked by small-amplitude and high-frequency waves in the EEG trace accompanied by frequent muscle activity episodes. Spectrograms were generated based on the multi-taper approach[12], and the power spectrum for each brain states was derived from the FFT as described above and previously[12,58].

Statistical analysis

To facilitate the comparison of power spectra across brain states and experimental treatment, 95% confidence intervals were constructed based on the t distribution (for EEG traces) or bootstrap method (for hippocampal field potentials, with 10,000 iterations). To compare the CSF tracer infiltration and molecular clearance across two hemispheres within the same animal, paired t-test was adapted. For the comparison of tracer intensity across different animals, Mann–Whitney test was used. To compare the Fos$^+$ cells, GFAP signals and biotin coverage in the blood–brain barrier assay across two hemispheres within the same animal, paired t-test was adapted. To compare the spike rate and instant amplitude of field potentials across experimental groups, Wilcoxon signed-rank test was used. To analyse brain perfusion across time between experiment groups in the MRI experiment, two-way repeated measures ANOVA was used. Statistical analysis was performed using Prism (GraphPad) and Matlab (MathWorks).

Reporting summary

Further information on research design is available in the Nature Portfolio Reporting Summary linked to this article.

Data availability

All data necessary for the conclusions of the study are available in the main text, figures and extended data. Representative raw widefield and MRI images are available from Zenodo (https://doi.org/10.5281/zenodo.10440376). Source data are provided with this paper.

Code availability

The Matlab codes used in this study are available from Zenodo (https://doi.org/10.5281/zenodo.10440376).

50. Drieu, A. et al. Parenchymal border macrophages regulate the flow dynamics of the cerebrospinal fluid. *Nature* **611**, 585–593 (2022).
51. Franklin, K. B. J. & Paxinos, G. *The mouse brain in stereotaxic coordinates* 4th edn (Academic Press, 2013).
52. Ayloo, S. et al. Pericyte-to-endothelial cell signaling via vitronectin-integrin regulates blood–CNS barrier. *Neuron* **110**, 1641–1655.e6 (2022).
53. Araragi, N., Alenina, N. & Bader, M. Carbon-mixed dental cement for fixing fiber optic ferrules prevents visually triggered locomotive enhancement in mice upon optogenetic stimulation. *Heliyon* **8**, e08692 (2022).
54. Kass, R. E., Eden, U. T. & Brown, E. N. *Analysis of Neural Data* (Springer, 2014).
55. Kramer, M. A. & Eden, U. T. *Case studies in neural data analysis: a guide for the practicing neuroscientist* (The MIT Press, 2016).
56. Cohen, M. X. *Analyzing neural time series data: theory and practice* (The MIT Press, 2014).
57. Rossant, C. et al. Spike sorting for large, dense electrode arrays. *Nat. Neurosci.* **19**, 634–641 (2016).
58. Prerau, M. J., Brown, R. E., Bianchi, M. T., Ellenbogen, J. M. & Purdon, P. L. Sleep neurophysiological dynamics through the lens of multitaper spectral analysis. *Physiology* **32**, 60–92 (2017).

Acknowledgements We thank S. Smith for editing the manuscript; A. Impagliazzo for her help on the illustration for Extended Data Fig. 9d; E. Griffin and A. Apaw for handling the mouse colony; S. Brophy for laboratory management; J. Quirk for his guidance on the acquisition and analysis of MRI images; and members of the Kipnis Laboratory for comments and suggestions. This study is supported by National Institutes of Health (NIH) DP1AT010416 (to J.K.), R01AT011419 (to J.K.), Barnes–Jewish Hospital investigators program (to J.K.) from Washington University School of Medicine, and a gift from the Neuroscience Innovation Foundation.

Author contributions L.-F.J.-X. conceived the original idea, designed and performed most of the experiments and analysed the data. A.D. helped design, execute and analyse MRI images. K.B. helped with stereotaxic surgeries, brain sectioning using the cryostat microtome, immunofluorescence staining, widefield imaging and data analysis. D.Q. helped with cryostat sectioning and widefield imaging. I.S. helped with surgical procedures, maintaining the mouse colony and post-surgery care of animals. J.K. participated in experimental design, provided intellectual guidance, resources and supervised the entire study. L.-F.J.-X. and J.K. wrote the paper with the input from all authors.

Competing interests J.K. is a co-founder of Rho Bio. The other authors declare no competing interests.

Additional information

Supplementary information The online version contains supplementary material available at https://doi.org/10.1038/s41586-024-07108-6.

Correspondence and requests for materials should be addressed to Li-Feng Jiang-Xie or Jonathan Kipnis.

Peer review information *Nature* thanks Axel Montagne and the other, anonymous, reviewer(s) for their contribution to the peer review of this work.

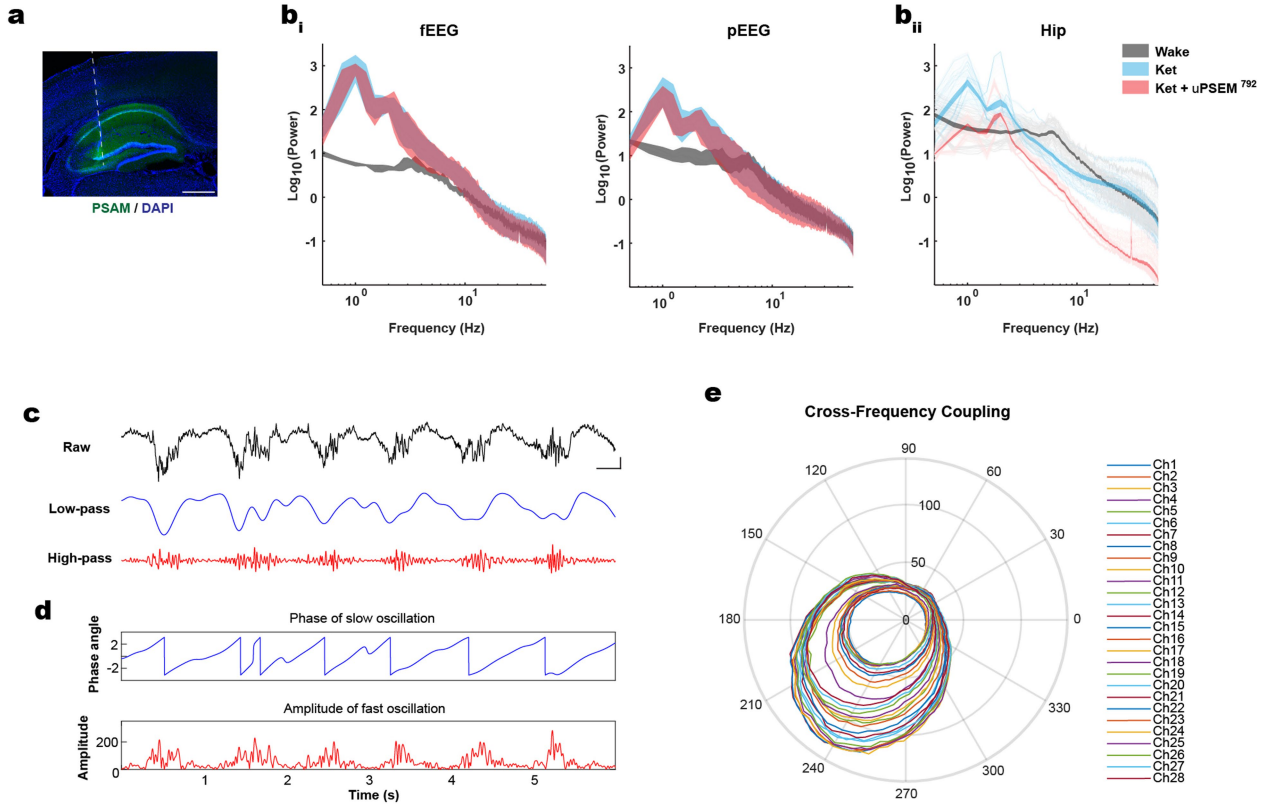

Extended Data Fig. 1 | Characterization of EEGs and ionic waves in ISF of hippocampus during wake and ketamine anesthesia with chemogenetic manipulation. a, Schematic of electrode location in PSAM-expressed hippocampus. **b**$_{i}$, Power spectra of frontal EEG (fEEG) and parietal EEG (pEEG) during wake, ketamine anesthesia (Ket) and Ket + uPSEM^{792}. n = 5 mice for wake; n = 4 mice for Ket and Ket + uPSEM^{792}. Shaded areas denote 95 percent confidence intervals for the mean. **b**$_{ii}$, Power spectra of ISF waves in hippocampus during wake, ketamine anesthesia with or without chemogenetic inhibition. n = 136 channes from 5 mice. Shaded areas denote 95 percent confidence intervals for the mean. **c-e**, Cross-frequency coupling analysis in hippocampal ISF during ketamine anesthesia, scale bar: 300 ms and 200 μV. Raw and filter traces (c), phase and power extraction (**d**), and polar plot across all 28-recording channels (**e**).

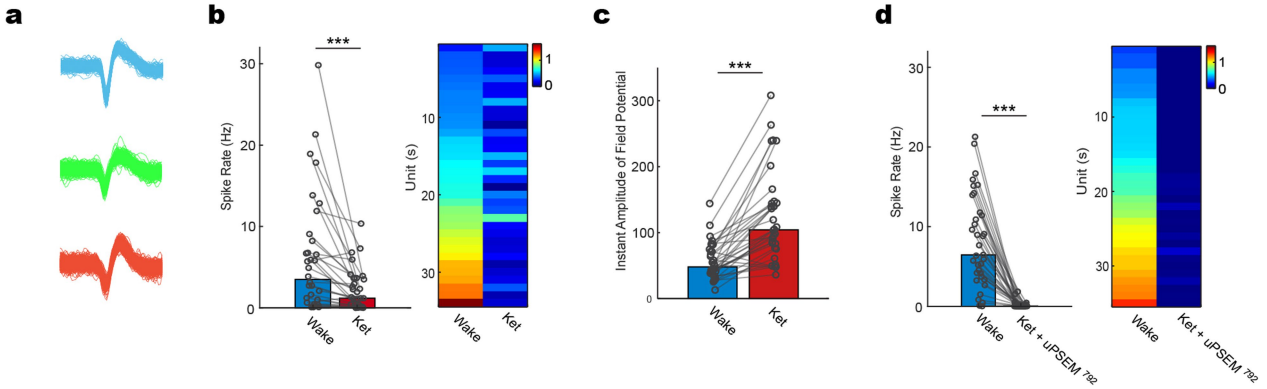

Extended Data Fig. 2 | Analysis of neuronal spikes in hippocampus during wake and ketamine anesthesia with chemogenetic perturbation. **a**, Examples of spike waveforms. **b**, Spike rate for isolated units during wakefulness and ketamine (n = 34 units from 5 mice). Left, statistical summary of unit spike rates; right, normalized activity heatmap. Two-sided Wilcoxon signed-rank test. $p < 0.0001$. **c**, Instant amplitude of field potential coupled with neuronal spikes (n = 34 units from 5 mice). Two-sided Wilcoxon signed-rank test. $p < 0.0001$. **d**, Spike rate for isolated units during wakefulness and ketamine with chemogenetic inhibition (n = 35 units from 5 mice). Left, statistical summary of unit spike rates; right, normalized activity heatmap. Two-sided Wilcoxon signed-rank test. $p < 0.0001$. *** $p < 0.001$.

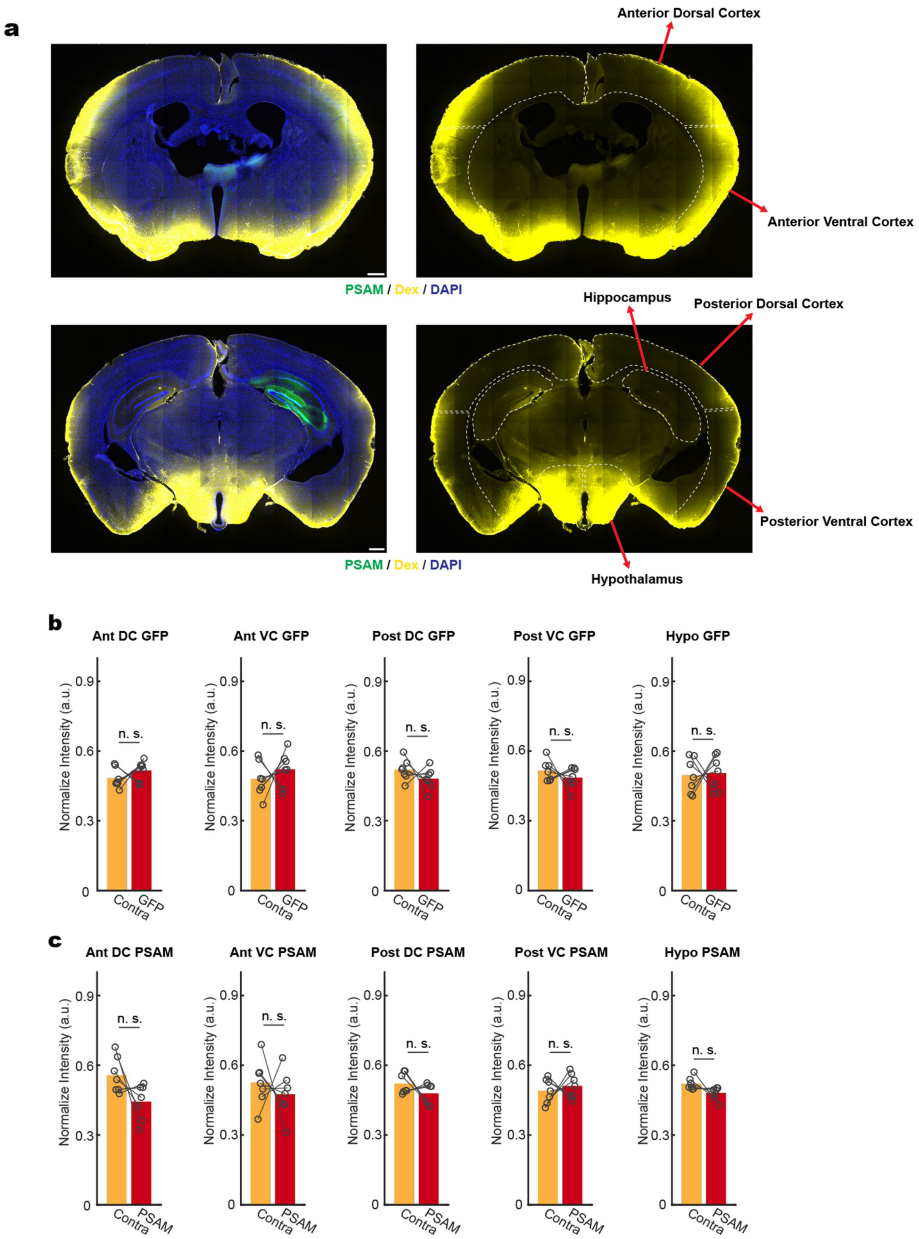

Extended Data Fig. 3 | Molecular infiltration analysis on additional brain regions. a, Representative images from PSAM-expressing animals. Left column displays composite images (GFP, Dex, and DAPI) from anterior to posterior (top to bottom); while the right column shows corresponding tracer-only (Dex) images. Statistical summary for tracer infiltration in GFP group. (**b**) and PSAM group (**c**) across multiple brain regions: Ant DC, anterior dorsal cortex; Ant VC, anterior ventral cortex; Post DC, posterior dorsal cortex; Post VC, posterior ventral cortex; Hypo, hypothalamus. n = 7 mice for both GFP and PSAM groups. Scale bar: 500 μm. Two-sided Paired-t test. n.s., not significant.

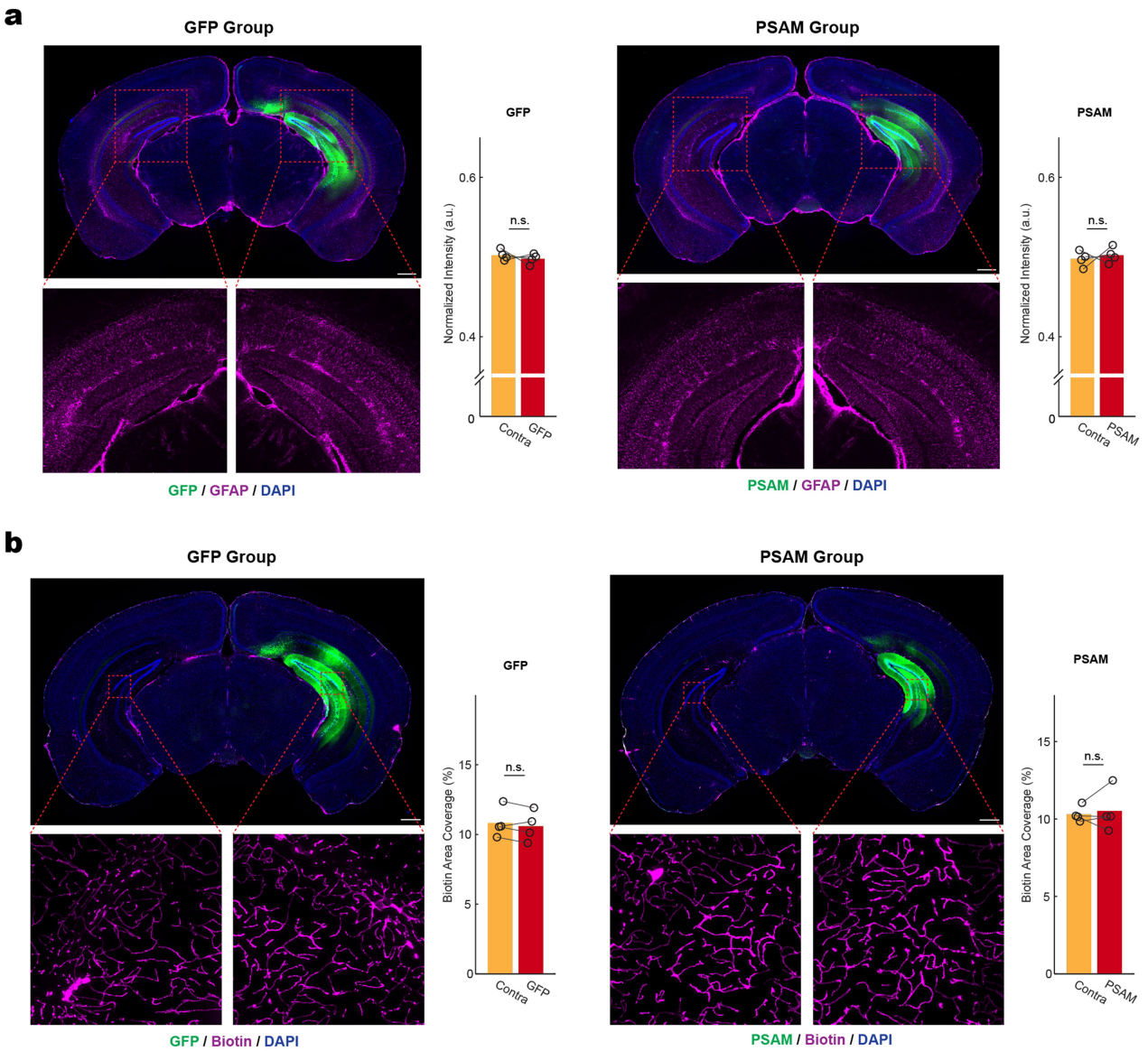

Extended Data Fig. 4 | Acute neuronal inhibition does not affect GFAP expression and blood-brain barrier integrity. a, GFAP staining after uPSEM^{792} treatment (3 mg/kg, i.p.) in GFP group (left panel, n = 4) and PSAM group (right panel, n = 4). GFAP, glial fibrillary acidic protein. Scale bar: 500 µm. Paired-t test. n.s., not significant. **b**, Blood-brain barrier leakage assay after uPSEM^{792} treatment (3 mg/kg, i.p.) in GFP group (left panel, n = 4) and PSAM group (right panel, n = 4). Scale bar: 500 µm. Two-sided paired-t test. n.s., not significant.

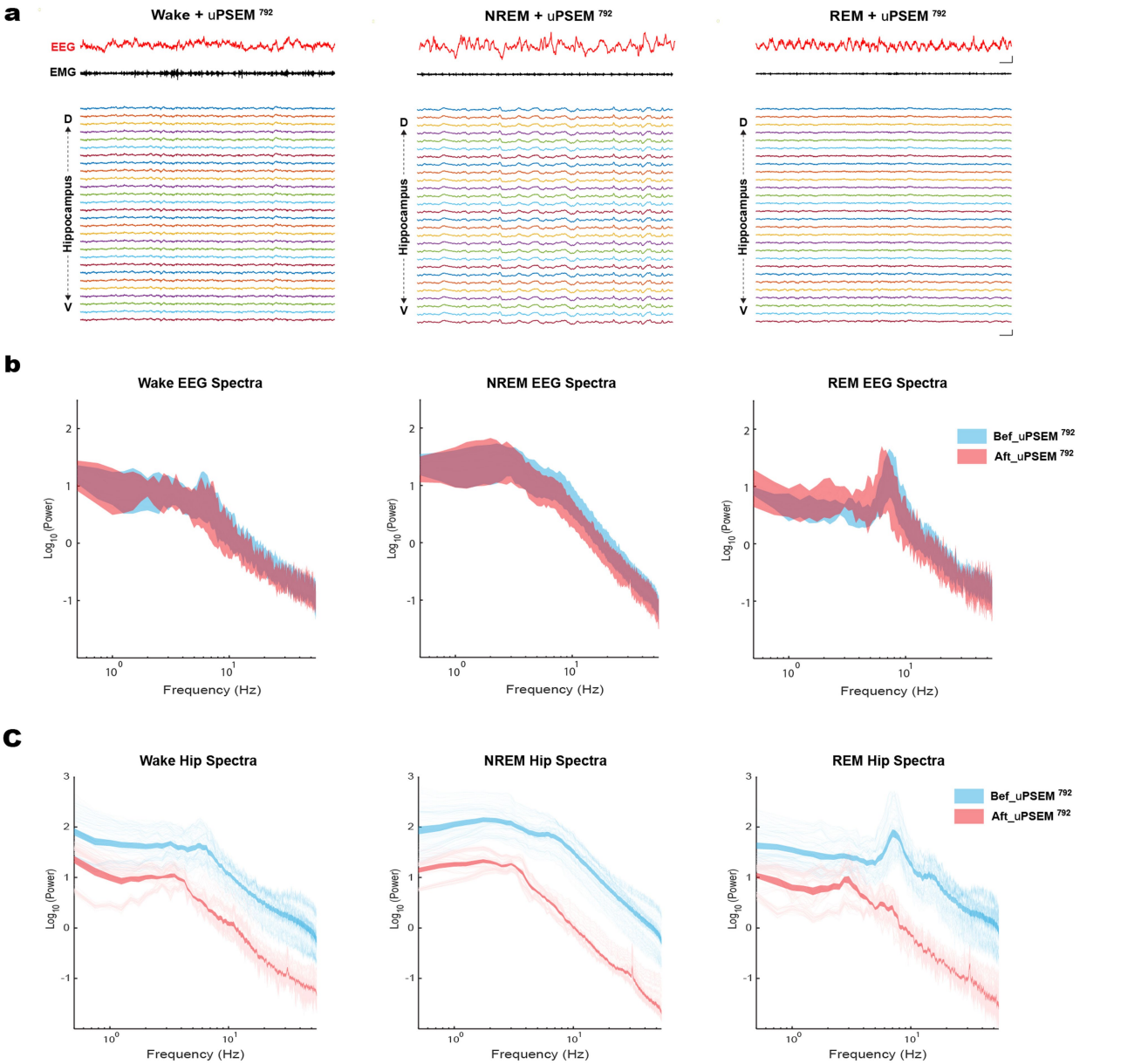

Extended Data Fig. 5 | Characterization of EEGs and ISF waves in hippocampus during natural sleep-wake cycle with chemogenetic inhibition. a, Representative traces of EEG, EMG, and ionic waves in the hippocampus during wake, NREM, and REM with chemogenetic inhibition. Top right scale bar: 200 ms and 200 μV for EEGs; bottom right scale bar: 200 ms and 200 μV for LFPs. **b**, Power spectra of cortical EEGs (n = 4 animals) before and after chemogenetic inhibition. **c**, Power spectra of hippocampal ISF before (n = 111 channels from 4 animals) and after (n = 109 channels from 4 animals) chemogenetic inhibition. Shaded areas denote 95 percent confidence intervals for the mean.

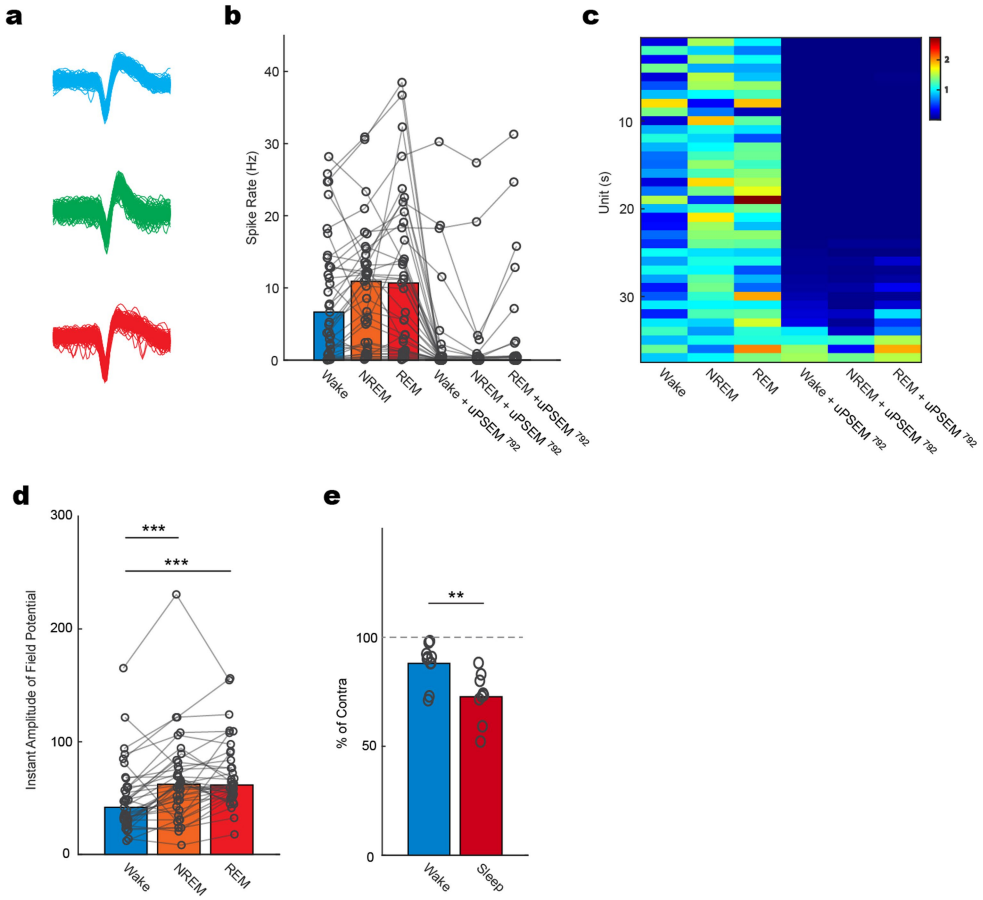

Extended Data Fig. 6 | Analysis of neuronal spikes in hippocampus during natural sleep-wake cycle with chemogenetic perturbation, the asymmetry of CSF perfusion between sleep and wake. a, Examples of spike waveforms. **b-c**, Spike rate for isolated units (n = 37 units from 4 mice) underlying wake, NREM, and REM with chemogenetic inhibition. **b**, Statistical summary of unit spike rates; **c**, Normalized activity heatmap. **d**, Instant amplitude coupled with neuronal spikes (n = 37 units from 4 mice). Two-sided Wilcoxon signed-rank test with Bonferroni correction. p = 0.0001 (Wake vs NREM) and p < 0.0001 (Wake vs REM) **e**, Asymmetry of CSF perfusion between wake (n = 10 animals) and sleep (n = 9 animals) conditions measured as percentage of contralateral (Contra) side. Two-sided Student t-test. p = 0.0045. $^{**}p < 0.01$, $^{***}p < 0.001$.

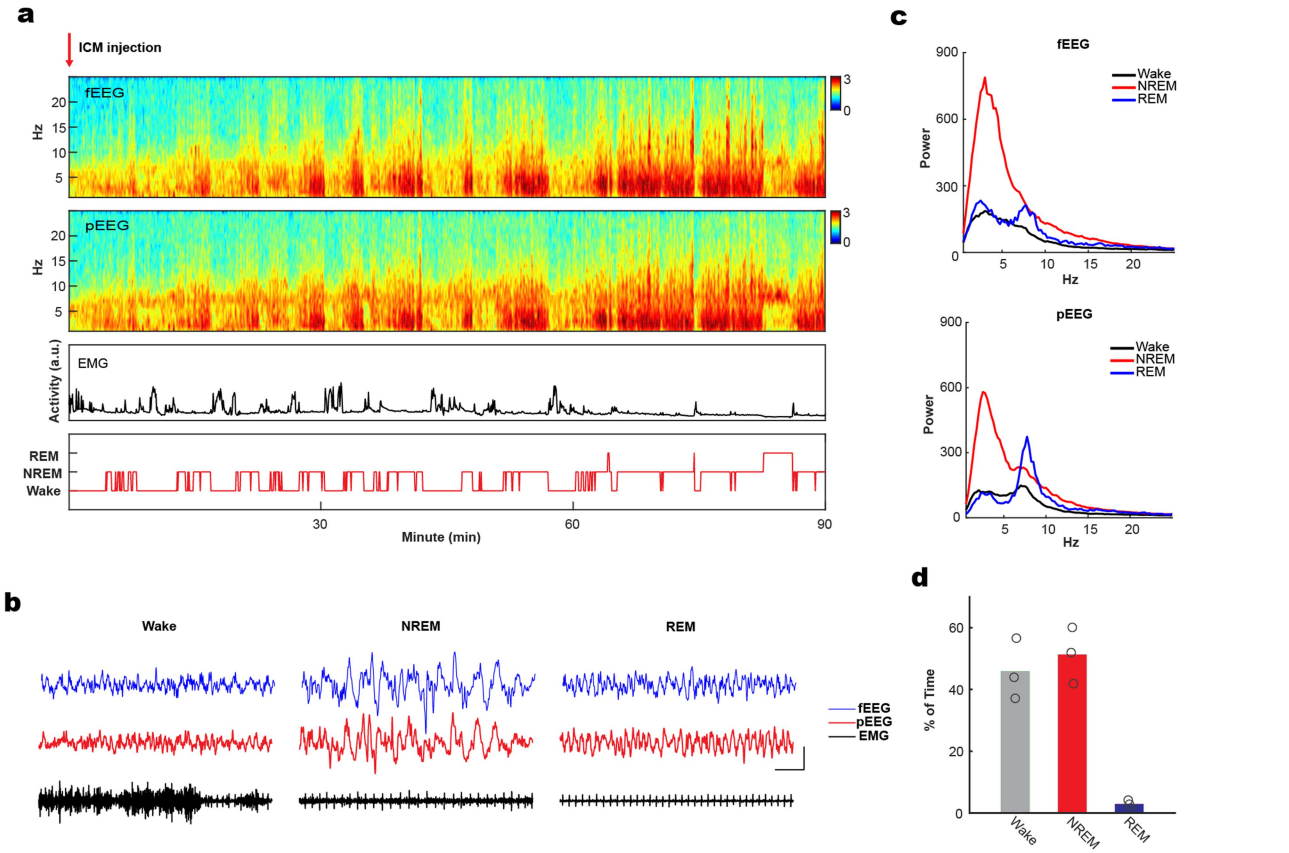

Extended Data Fig. 7 | EEG/EMG characterization after acute intracisterna magna (ICM) injection. a, Representative spectrograms from fEEG (top row), pEEG (second row), EMG (third row), hypnogram (fourth row) after acute ICM injection. **b**, Representative recording traces in three different brain states, wake, NREM, and REM. Blue trace, fEEG; red trace, pEEG, black trace, EMG. Scale bar: 500 ms and 200 μV. **c**, Power spectrum analysis across wake, NREM, and REM in the frontal EEG (top) and parietal (bottom) EEG channels. **d**, Percentage of time spent in Wake, NREM, and REM sleep., n = 3 animals. fEEG, frontal EEG; pEEG, parietal EEG.

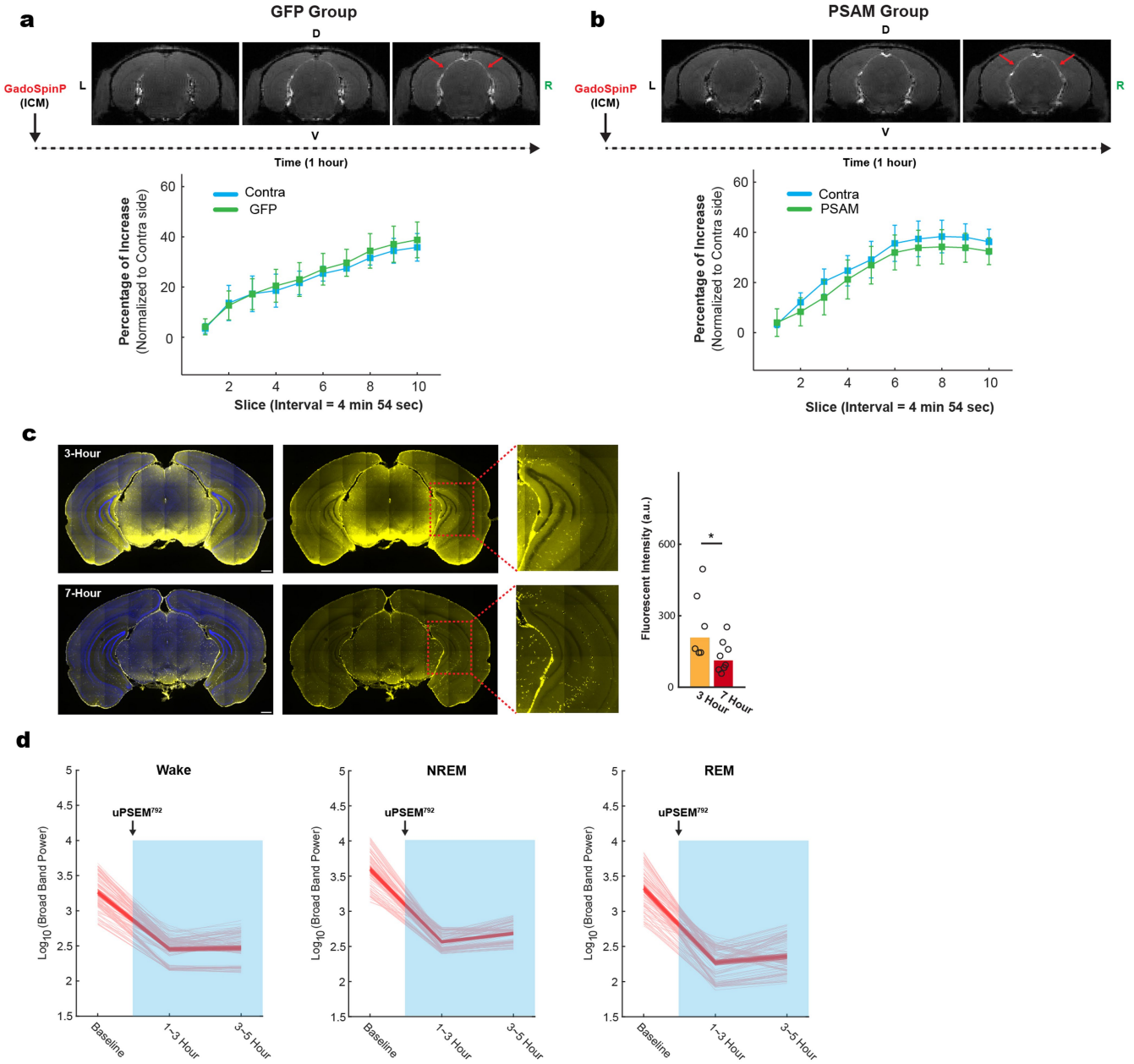

Extended Data Fig. 8 | MRI, the time window for molecular clearance, and the efficacy and duration of chemogenetic inhibition. a-b, Paravascular flow is largely preserved during local neuronal inhibition in hippocampus. Left panel, GFP group; right panel, PSAM group. GadoSpinP, large molecular tracer (~200 kDa) used to visualize para-vascular flow. ICM, intracisterna magna injection. n = 3 mice for GFP group; n = 4 mice for PSAM group. Data presented as mean ± s.e.m. **c**, 3–7 h after ICM (3 kD Dextran-TexasRed, yellow) injection mainly captures molecular clearance phase. n = 6 mice for 3-hour group; n = 8 mice for 7-hour group. Two-sided Mann-Whitney test, p = 0.0426. Scar bar = 500 µm. **d**, Chemogenetic inhibition lasts for 5 h after uPSEM^{792} injection across three brain states, wake, NREM, REM. n = 109 channels from 4 animals. Shaded areas denote 95 percent confidence intervals for the mean. *$p < 0.05$.

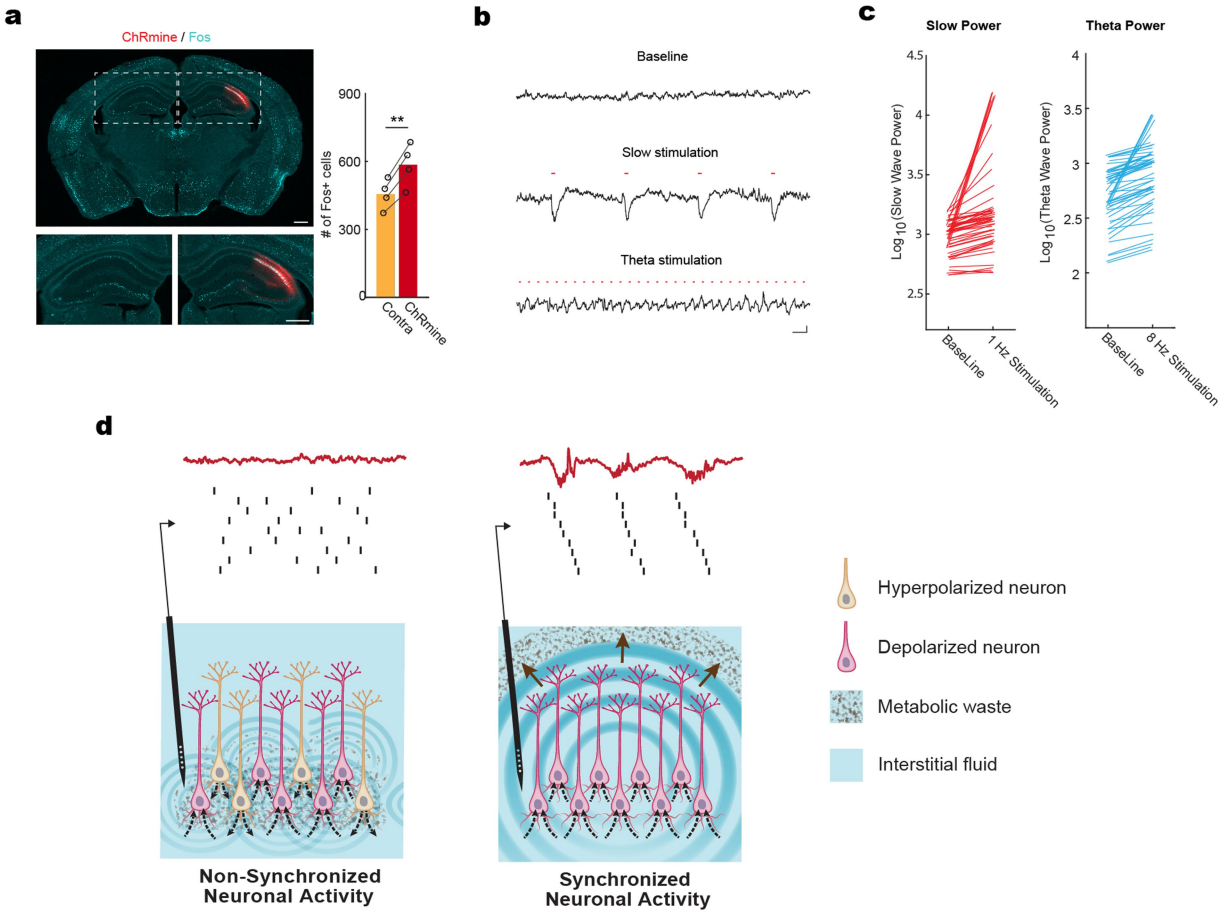

Extended Data Fig. 9 | Validation of optogenetic toolkits. a, Transcranial activation of neurons revealed by Fos staining. Left, representative images; right, statistical summary (n = 4 animals). Contra, contralateral side of the hippocampus. Scale bar: 500 μm. Two-sided paired-t test. p = 0.0031. **b**, Representative field potential traces with photo-stimulations in ChRmine-expressing animals. Slow stimulation: 1 Hz, 50 ms per TTL pulse; theta stimulation: 8 Hz, 6.25 ms per TTL pulse. Scale bar: 200 ms and 300 μV. **c**, Quantification of slow wave (0.5–4 Hz) power and theta wave (6–10 Hz) power from optrode recording experiment (n = 54 channels from 2 animals). **d**, Illustration of the principle that neurons firing together shower together. $^{**}p < 0.01$.

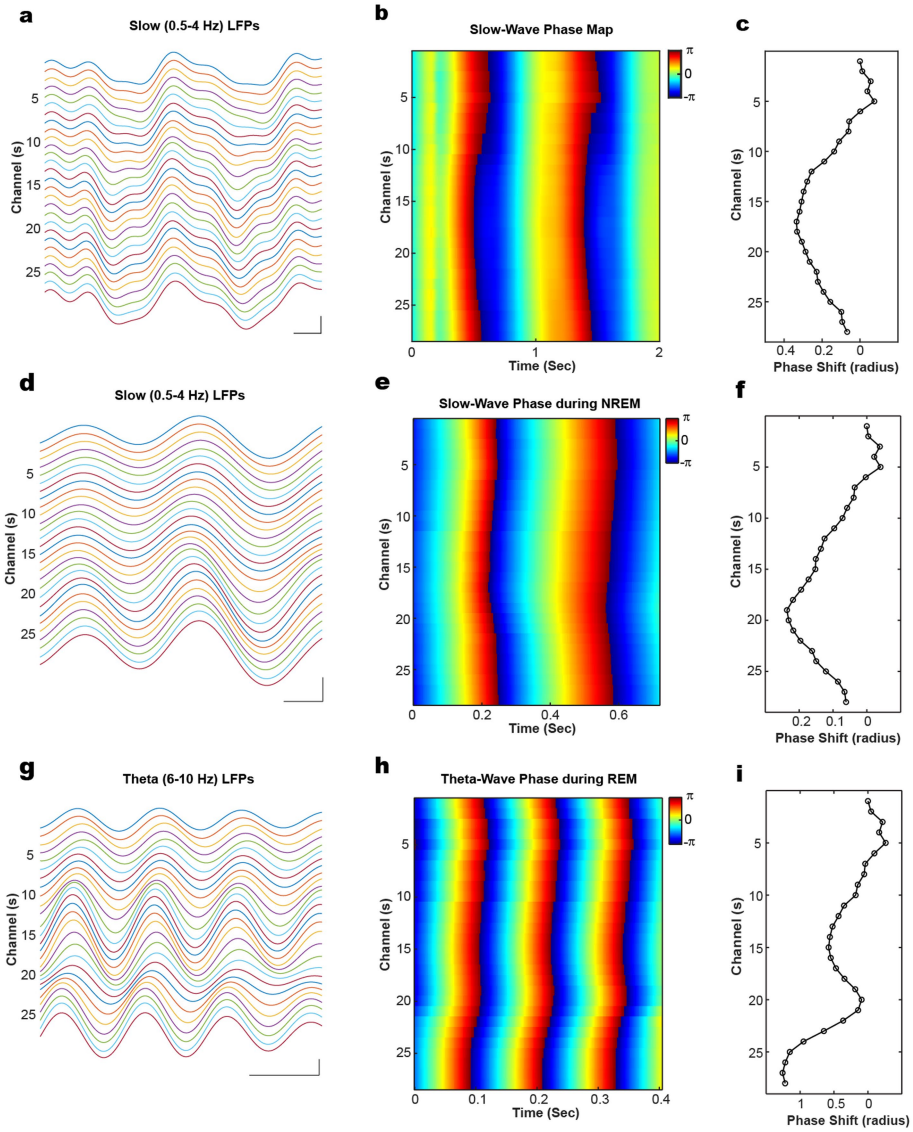

Extended Data Fig. 10 | Wave phase progression analysis across electrophysiological recording channels in hippocampus during different brain states. a-c, Representative slow (0.5–4 Hz) filtered traces (**a**) from hippocampal field potential recordings during ketamine anesthesia, corresponding phases (**b**) extracted with Hilbert method, and averaged phase shift (**c**). Scale bar: 200 ms and 200 μV. **d-f**, Representative slow (0.5–4 Hz) filtered traces (**d**) from hippocampal field potential recordings during NREM sleep, corresponding phases (**e**) extracted with Hilbert method, and averaged phase shift (**f**). Scale bar: 100 ms and 200 μV. **g-i**, Representative theta (6–10 Hz) filtered traces (**g**) from hippocampal field potential recordings during REM sleep, corresponding phases (**h**) extracted with Hilbert method, and averaged phase shift (**i**). Scale bar: 100 ms and 200 μV.

nature portfolio

Corresponding author(s): Li-Feng Jiang-Xie & Jonathan Kipnis

Last updated by author(s): Nov 29, 2023

Reporting Summary

Nature Portfolio wishes to improve the reproducibility of the work that we publish. This form provides structure for consistency and transparency in reporting. For further information on Nature Portfolio policies, see our Editorial Policies and the Editorial Policy Checklist.

Statistics

For all statistical analyses, confirm that the following items are present in the figure legend, table legend, main text, or Methods section.

n/a	Confirmed	
☐	☒	The exact sample size (*n*) for each experimental group/condition, given as a discrete number and unit of measurement
☐	☒	A statement on whether measurements were taken from distinct samples or whether the same sample was measured repeatedly
☐	☒	The statistical test(s) used AND whether they are one- or two-sided *Only common tests should be described solely by name; describe more complex techniques in the Methods section.*
☒	☐	A description of all covariates tested
☐	☒	A description of any assumptions or corrections, such as tests of normality and adjustment for multiple comparisons
☐	☒	A full description of the statistical parameters including central tendency (e.g. means) or other basic estimates (e.g. regression coefficient) AND variation (e.g. standard deviation) or associated estimates of uncertainty (e.g. confidence intervals)
☐	☒	For null hypothesis testing, the test statistic (e.g. *F*, *t*, *r*) with confidence intervals, effect sizes, degrees of freedom and *P* value noted *Give P values as exact values whenever suitable.*
☒	☐	For Bayesian analysis, information on the choice of priors and Markov chain Monte Carlo settings
☒	☐	For hierarchical and complex designs, identification of the appropriate level for tests and full reporting of outcomes
☒	☐	Estimates of effect sizes (e.g. Cohen's *d*, Pearson's *r*), indicating how they were calculated

Our web collection on statistics for biologists contains articles on many of the points above.

Software and code

Policy information about availability of computer code

Data collection	Electrophysiology data were collected with Tucker-Davis Technologies (TDT) RZ2 with SYNAPSE software or EEG/EMG system from Pinnacle Technology (# 8200-K1-SL); Images were acquired using Olympus SLIDEVIEW VS200; MRI data were collected using Bruker 9.4 Tesla.
Data analysis	FIJI image (2.9.0) processing software (NIH), Prism 9 (GraphPad), MATLAB 2020a (MathWorks), ITK-SNAP (3.6.0), Kilosort 2.5, Phy GUI

For manuscripts utilizing custom algorithms or software that are central to the research but not yet described in published literature, software must be made available to editors and reviewers. We strongly encourage code deposition in a community repository (e.g. GitHub). See the Nature Portfolio guidelines for submitting code & software for further information.

Data

Policy information about availability of data

All manuscripts must include a data availability statement. This statement should provide the following information, where applicable:

- Accession codes, unique identifiers, or web links for publicly available datasets
- A description of any restrictions on data availability
- For clinical datasets or third party data, please ensure that the statement adheres to our policy

All data necessary for the conclusions of the study are available in the main text, figures, and extended data. The source data for each main figure and extended data figure are all provided. Representative raw wield-field and MRI images, as well as MATLAB codes are also available in Zenodo (https://doi.org/10.5281/zenodo.10440376)

Human research participants

Policy information about studies involving human research participants and Sex and Gender in Research.

Reporting on sex and gender	N/A
Population characteristics	N/A
Recruitment	N/A
Ethics oversight	N/A

Note that full information on the approval of the study protocol must also be provided in the manuscript.

Field-specific reporting

Please select the one below that is the best fit for your research. If you are not sure, read the appropriate sections before making your selection.

☒ Life sciences ☐ Behavioural & social sciences ☐ Ecological, evolutionary & environmental sciences

For a reference copy of the document with all sections, see nature.com/documents/nr-reporting-summary-flat.pdf

Life sciences study design

All studies must disclose on these points even when the disclosure is negative.

Sample size	No statistical methods were used to determine the sample size in advance. The number of animals used in this study was largely based on previous studies from our lab and others (Drieu et al. 2022; Iliff et al. 2012).
Data exclusions	No data were excluded from experiments unless apparent failures, such as failure of intra-cisterna magna and intraperenchymal injections.
Replication	All experiments were replicated in at least three independent experiments for a total of at least 3 mice per group, and all attempts to replicate the data were successful.
Randomization	Animals were randomly assigned to the experimental or control group.
Blinding	The researchers were blind to the group allocation during data acquisition and analysis.

Reporting for specific materials, systems and methods

We require information from authors about some types of materials, experimental systems and methods used in many studies. Here, indicate whether each material, system or method listed is relevant to your study. If you are not sure if a list item applies to your research, read the appropriate section before selecting a response.

Materials & experimental systems

n/a	Involved in the study
☐	☒ Antibodies
☒	☐ Eukaryotic cell lines
☒	☐ Palaeontology and archaeology
☐	☒ Animals and other organisms
☒	☐ Clinical data
☒	☐ Dual use research of concern

Methods

n/a	Involved in the study
☒	☐ ChIP-seq
☒	☐ Flow cytometry
☐	☒ MRI-based neuroimaging

Antibodies

Antibodies used	c-Fos (9F6) primary antibody (Cell Signaling Technology #2250), GFAP (Agilent Technologies Z033429-2)
Validation	c-Fos: Osterhout et al., Nature 606, pages 937-944(2022); GFAP: Li et al., Nature 587, pages 613–618 (2020)

Animals and other research organisms

Policy information about studies involving animals; ARRIVE guidelines recommended for reporting animal research, and Sex and Gender in Research

Laboratory animals	C57BL/6J mice, 2-6 months old. Animals were housed inside a temperature (22 ºC) and humidity-controlled (33 - 39 %) environment with 12-hour light/dark cycle and provided with food and water ad libitum.
Wild animals	No wild animals were used in this study.
Reporting on sex	Male mice were used in this study.
Field-collected samples	No field-collected samples.
Ethics oversight	All experimental procedures were approved by the Institutional Animal Care and Used Committee in Washington University School of Medicine.

Note that full information on the approval of the study protocol must also be provided in the manuscript.

Magnetic resonance imaging

Experimental design

Design type	Evaluation of CSF infiltration across time using Dotarem and Gadospin P
Design specifications	The total acquisition time is about 1 hour per mouse (4 minutes 54 seconds X 11 sequences)
Behavioral performance measures	None

Acquisition

Imaging type(s)	Contrast-enhanced MRI
Field strength	9.4 Tesla
Sequence & imaging parameters	A series of T1 FLASH-3D weighted images were taken to visualize CSF perfusion with the following parameters: repetition time = 30 ms; echo time = 8 ms; number of echo images = 1; number of averages = 1; number of repetitions = 11; scan time = 4 minutes and 54 seconds; flip angle = 20, FOV = 1.6 x 1.6 x 0.8 cm with a 128 x 128 x 64 matrix ; spatial resolution = 125 x 125 x 125 µm (8 pixels per mm; voxel size = 0.125 mm3), number of slices = 64; receiving coil: 4-channel brain probe.
Area of acquisition	Mouse brain

Diffusion MRI ☐ Used ☒ Not used

Preprocessing

Preprocessing software	Paravision 360
Normalization	Each mouse served as its own control
Normalization template	Each mouse served as its own control (tracer infiltration over time)
Noise and artifact removal	No noise or artifact removal
Volume censoring	None

Statistical modeling & inference

Model type and settings	Tracer diffusion across time for each mouse
Effect(s) tested	Two-way repeated measure ANOVA

Specify type of analysis: ☐ Whole brain ☒ ROI-based ☐ Both

Anatomical location(s): Mouse hippocampus and its nearby perivascular pathways

Statistic type for inference (See Eklund et al. 2016): *Specify voxel-wise or cluster-wise and report all relevant parameters for cluster-wise methods.*

Correction | *Describe the type of correction and how it is obtained for multiple comparisons (e.g. FWE, FDR, permutation or Monte Carlo).*

Models & analysis

n/a	Involved in the study
☒	☐ Functional and/or effective connectivity
☒	☐ Graph analysis
☒	☐ Multivariate modeling or predictive analysis